

A multi-dimensional implementation of the Advanced Spectral neutrino Leakage scheme

D. Gizzi,^{1*} E. O’Connor,¹ S. Rosswog,¹ A. Perego,^{2,3} R. M. Cabezón,⁴ L. Nativi¹

¹*Department of Astronomy & The Oskar Klein Centre, Stockholm University, AlbaNova, 106 91, Stockholm, Sweden*

²*Dipartimento di Fisica, Università degli Studi di Trento, via Sommarive 14, 38123 Trento, Italy*

³*INFN, Sezione di Milano-Bicocca, Piazza della Scienza 3, 20126 Milano, Italy*

⁴*Center for Scientific Computing - sciCORE, University of Basel, Klingelbergstrasse 61, CH-4056 Basel, Switzerland*

Accepted XXX. Received YYY; in original form ZZZ

ABSTRACT

We present a new, multi-dimensional implementation of the Advanced Spectral Leakage (ASL) scheme with the purpose of modelling neutrino-matter interactions in neutron star mergers. A major challenge is the neutrino absorption in the semi-transparent regime, which is responsible for driving winds from the merger remnant. The composition of such winds is crucial in the understanding of the electromagnetic emission in the recently observed macronova following GW170817. Compared to the original version, we introduce an optical-depth-dependent flux factor to model the average angle of neutrino propagation, and a modulation that accounts for flux anisotropies in non-spherical geometries. We scrutinise our approach by first comparing the new scheme against the original one for a spherically symmetric core-collapse supernova snapshot, both in 1D and in 3D, and additionally against a two-moment (M1) scheme as implemented in 1D into the code GR1D. The luminosities and mean energies agree to a few percents in most tests. Finally, for the case of a binary merger remnant snapshot we compare the new ASL scheme with the M1 scheme that is implemented in the Eulerian adaptive mesh refinement code FLASH. We find that the neutrino absorption distribution in the semi-transparent regime is overall well reproduced. Both approaches agree to within $\lesssim 15\%$ for the average energies and to better than $\sim 35\%$ in the total luminosities.

Key words: neutrinos, radiative transfer, hydrodynamics, star: neutron, stars: supernovae: general

1 INTRODUCTION

The first multi-messenger detection of a neutron star merger (Abbott et al. 2017c) has brought major leaps forwards for many areas of (astro)physics. For example, the 1.7s delay between the gravitational wave (GW) peak and the gamma-rays from an event detected by the Fermi satellite (Goldstein et al. 2017) allowed to constrain the deviations of the GW propagation speed from the speed of light to 1 part in 10^{15} (Abbott et al. 2017c). The detection further allowed for an independent measure of the Hubble parameter (Abbott et al. 2017b) as suggested by Schutz (1986). The GW signal was followed by emission all across the electromagnetic (EM) spectrum (e.g. Arcavi et al. 2017; Chornock et al. 2017; Kasliwal et al. 2017; Kilpatrick et al. 2017; Kasen et al. 2017; Pian et al. 2017; Smartt et al. 2017; Abbott et al. 2017c,a; Goldstein et al. 2017; Savchenko et al. 2017; Coulter et al.

2017; Troja et al. 2017; Margutti et al. 2017; Haggard et al. 2017; Alexander et al. 2017; Hallinan et al. 2017; Tanvir et al. 2017). The intensity of the EM emission detected in the aftermath of the event decayed with a power-law exponent close to -1.3 (Kasliwal et al. 2017; Rosswog et al. 2018) as expected for a distribution of freshly synthesised r-process elements (Metzger et al. 2010; Korobkin et al. 2012). Estimates of the involved ejecta masses point to $\sim 0.02 M_{\odot}$ for the early blue emission component and $\sim 0.04 M_{\odot}$ for the later emerging red component (Villar et al. 2017; Kasen et al. 2017; Perego et al. 2017b; Rosswog et al. 2018). The early blue component requires lanthanide-free ejecta which, in turn, are the r-process nucleosynthesis result of matter with $Y_e \gtrsim 0.25$ (Korobkin et al. 2012; Kasliwal et al. 2019) (ejected at velocities of $\sim 0.3c$). The later emerging, red component stems from matter with electron fractions below this threshold value. Since the original neutron stars are in β -equilibrium they contain only about $10^{-4} M_{\odot}$ of matter with $Y_e > 0.25$. Therefore, the observed $\sim 2\%$ of a solar mass

* E-mail: davide.gizzi@astro.su.se

in the blue component point to a major re-processing of a large fraction of the ejecta by weak interactions, raising Y_e via $e^+ + n \rightarrow p + \bar{\nu}_e$ and $\nu_e + n \rightarrow p + e^-$. With GW170817 and its EM emission we have thus witnessed weak interaction “in flagranti”. This underlines the paramount importance of carefully modelling weak interactions and neutrino physics in a neutron star merger for reliable predictions of their EM signature.

Addressing the neutrino transport problem by solving the full multi-dimensional Boltzmann equation (Lindquist 1966) is computationally very demanding and for most astrophysical problems it is prohibitively expensive. Therefore, most multi-dimensional hydrodynamic studies, both for supernovae and compact binary mergers resort to transport approximations (e.g. Thorne 1981; Bruenn et al. 1978; Mezzacappa & Messer 1999; Bruenn 1985; Rosswog & Liebendörfer 2003; Buras et al. 2006; O’Connor & Couch 2018; Dessart et al. 2009; Foucart et al. 2016; Perego et al. 2017a; Ardevol-Pulpillo et al. 2019; Cabezón et al. 2018). Our particular focus here is on the Advanced Spectral Leakage (hereafter ASL) (Perego et al. 2016), that has recently been scrutinised against more expensive neutrino treatments (Pan et al. 2018) in a core-collapse supernova context. Since supernovae are roughly spherically symmetric, they allow for approximations that are not admissible in a neutron star merger context. In this paper we extend the original ASL scheme to multi-dimensional applications, while keeping the general structure of the equations as presented in the original papers (Perego et al. 2014, 2016). We examine the modified scheme in typical core-collapse supernova and neutron star merger remnant snapshots. We focus on the modelling of the absorption in the semi-transparent regime, which is responsible for the neutrino-driven winds (Perego et al. 2014; Radice et al. 2018b), one of the possible ejection channels related to the observed blue EM component. We rely on a spectral treatment of the neutrino-matter interactions, a key ingredient for capturing the composition of the polar ejecta (Foucart et al. 2016). The ASL presented here allows for a computationally-inexpensive, spectral treatment of the neutrino absorption in the semi-transparent regime, and it is therefore suitable for long-term binary merger simulations, where more detailed neutrino treatments require larger computational resources.

The paper is structured as follows: in Sec. 2 we describe the ASL methodology both in its original 1D version (Sec. 2.1) and in our new multi-D implementation (Sec. 2.2). Simulation results are presented in Sec. 3. In Sec. 3.1 we start with a one-dimensional core-collapse profile. We then move to three-dimensional configurations in Sec. 3.2 where we first use the same core-collapse supernova profile to inspect our multi-D implementation of the ASL scheme. Finally, we apply the ASL to a neutron star merger remnant. In all cases, we scrutinise the ASL scheme by comparison with a two-moment (M1) scheme, and we neglect relativistic effects everywhere. In Sec. 4 we summarise our results.

2 THE ADVANCED SPECTRAL LEAKAGE

2.1 1D implementation

We first summarise the most relevant features of the ASL scheme for spherically symmetric systems, as they are de-

scribed in Perego et al. (2016). In their work, the ASL scheme is explored both in 1D and multi-D spherically symmetric core-collapse setups, showing flexibility and overall agreement with other neutrino transport models.

At the heart of the ASL approach is a spectral (i.e. energy-dependent) description of neutrino transport in which a neutrino energy spectrum is initially set up to account for the energy-squared dependence of neutrino-matter interactions. As in most approximate treatments, we model neutrinos as three independent species: electron neutrinos ν_e , electron anti-neutrinos $\bar{\nu}_e$, and a collective species for heavy-lepton neutrinos and anti-neutrinos ν_x . For the interactions between neutrinos and matter we consider the production and absorption of electron neutrinos and anti-neutrinos via charged current processes involving nucleons and nuclei, neutrino emission by bremsstrahlung and pair processes, and finally the scattering off nucleons and nuclei. These reactions enter the computation of the local optical depth $\tau_\nu(E, \mathbf{x})$ for an energy E at position \mathbf{x} , which is a measure of the average number of interactions a neutrino experiences before escaping to infinity and defined as integral of the inverse local mean free path $\lambda_\nu(E, \mathbf{x}')$ over a path γ

$$\tau_\nu(E, \mathbf{x}) = \int_{\gamma: \mathbf{x} \rightarrow +\infty} \frac{1}{\lambda_\nu(E, \mathbf{x}'(s))} ds. \quad (1)$$

Two different optical depths are defined: the first is the *total optical depth* $\tau_{\nu, \text{tot}}$ where both absorption and elastic scattering interactions are equally considered in the inverse mean free path calculation. The second is the *energy optical depth* $\tau_{\nu, \text{en}}$, which is related to the mean free path over which neutrinos can exchange energy with the fluid. An analytical estimate of the latter is given by computing the geometric mean between the total and the absorption inverse mean free paths:

$$\lambda_{\nu, \text{en}}(E, \mathbf{x}) = \sqrt{\frac{c \lambda_{\nu, \text{tot}}(E, \mathbf{x})}{\sum_s \chi_{\nu, \text{ab}, s}(E, \mathbf{x})}}, \quad (2)$$

where $\chi_{\nu, \text{ab}, s}(E, \mathbf{x})$ is the absorptivity of the absorption process ‘s’ and c is the speed of light. Each optical depth defines a *neutrino surface* at $\tau_\nu = 2/3$, where neutrinos begin to decouple from matter.

The net specific¹, spectral² neutrino emission rate (units of $\text{s}^{-1} \text{g}^{-1} \text{erg}^{-3}$) is initially calculated as a smooth interpolation between the production $r_{\nu, \text{prod}}(E, \mathbf{x})$ and diffusion $r_{\nu, \text{diff}}(E, \mathbf{x})$ rate

$$\tilde{r}_\nu(E, \mathbf{x}) = \frac{r_{\nu, \text{prod}}(E, \mathbf{x}) r_{\nu, \text{diff}}(E, \mathbf{x})}{r_{\nu, \text{prod}}(E, \mathbf{x}) + r_{\nu, \text{diff}}(E, \mathbf{x})}. \quad (3)$$

where $r_{\nu, \text{prod}}(E, \mathbf{x})$ depends on the production timescale $t_{\nu, \text{prod}}$, which in turn is set by the local emissivity, while $r_{\nu, \text{diff}}(E, \mathbf{x})$ depends on the timescale over which neutrinos diffuse out of the system, $t_{\nu, \text{diff}}$. This timescale is set by the local opacity via $\sim \tau_{\nu, \text{tot}}^2(E, \mathbf{x})$. Eq. (3) favours $r_{\nu, \text{diff}}(E, \mathbf{x})$ in optically thick conditions ($\tau_{\nu, \text{tot}}(E, \mathbf{x}) \gg 1$) and $r_{\nu, \text{prod}}(E, \mathbf{x})$ in optically thin conditions ($\tau_{\nu, \text{tot}}(E, \mathbf{x}) \lesssim 1$). We add two further corrections. First, when a large amount of neutrinos is emitted at the neutrino surface or is locally produced,

¹ To be explicit: we always use “specific” for quantities on a per mass basis.

² We always use “spectral” for quantities in units of $E^2 dE$.

Pauli blocking occurs as a consequence of the fermionic nature of neutrinos. Second, emission in optically thin regimes provided by $r_{\nu,\text{prod}}$ is assumed isotropic, and a fraction of neutrinos are emitted toward the optically thick regime. To account for these effects, neutrino emission is reduced by introducing a Pauli blocking parameter $\alpha_{\nu,\text{blk}}$: $\tilde{r}_{\nu} \rightarrow (1 - \alpha_{\nu,\text{blk}})\tilde{r}_{\nu}$. Second, during the diffusion process in the optically thick regime, neutrinos thermalize to lower energies and therefore the spectrum at the neutrino surface is softened. The softening of the spectrum is included via the term $\frac{1}{\Psi_{\nu}(\mathbf{x})}\exp(-\tau_{\nu,\text{en}}(E, \mathbf{x})/\tau_{\text{cut}})$, with $\Psi_{\nu}(\mathbf{x})$ defined as

$$\Psi_{\nu}(\mathbf{x}) = \frac{\int_0^{+\infty} \tilde{r}_{\nu}(E, \mathbf{x}) e^{-\tau_{\nu,\text{en}}(E, \mathbf{x})/\tau_{\text{cut}}} E^2 dE}{\int_0^{+\infty} \tilde{r}_{\nu}(E, \mathbf{x}) E^2 dE}, \quad (4)$$

where τ_{cut} parametrizes the typical number of interactions required to thermalize neutrinos. The equation for the neutrino emission rate finally becomes (we will occasionally refer to this emission as *cooling*)

$$r_{\nu}(E, \mathbf{x}) = (1 - \alpha_{\nu,\text{blk}})\tilde{r}_{\nu}(E, \mathbf{x}) \frac{1}{\Psi_{\nu}(\mathbf{x})} \exp(-\tau_{\nu,\text{en}}(E, \mathbf{x})/\tau_{\text{cut}}). \quad (5)$$

The values of $\alpha_{\nu,\text{blk}}$ and τ_{cut} are geometry-dependent, and must ideally be calibrated every time the system geometry changes significantly over the time of the simulation. A good trade-off is to provide fixed values for these parameters that are able to approximately reproduce the neutrino properties dynamically in comparison to other transport approaches. So far, $\alpha_{\nu,\text{blk}}$ and τ_{cut} have been calibrated in the context of spherically symmetric core-collapse supernovae simulations against full Boltzmann neutrino transport (Perego et al. 2016). Electron neutrinos and anti-neutrinos have $\alpha_{\nu,\text{blk}} \sim 0.55$. Heavy-lepton neutrinos are generally subdominant and their emission in optically thin regime is negligible, therefore $\alpha_{\nu,\text{blk}} \sim 0$. For the thermalization coefficient we adopt $\tau_{\text{cut}} = 20$ for all neutrino species. Although a new calibration in the context of binary merger simulations would be preferred, for the time being we assume the same values adopted for core-collapse simulations, leaving the detailed binary merger calibration task to a future work. The absorption of neutrinos in the optically thin regime is hereafter referred to as *heating*, and the specific, spectral absorption rate (units of $\text{s}^{-1}\text{g}^{-1}\text{erg}^{-3}$) is defined as

$$h_{\nu}(E, \mathbf{x}) = \frac{1}{\rho(\mathbf{x})} n_{\nu,\tau \lesssim 1} \chi_{\nu,\text{ab}} F_{e^{\pm}} H, \quad (6)$$

where $\rho(\mathbf{x})$ is the mass density of the fluid at position \mathbf{x} , $\chi_{\nu,\text{ab}}$ the absorptivity, $n_{\nu,\tau \lesssim 1}$ the neutrino number density in optically thin regime, $H = \exp(-\tau_{\nu,\text{tot}})$ ensures the heating to be applied only in the optically thin regime. All quantities on the RHS of Eq. (6) are functions of energy E and position \mathbf{x} . The Pauli blocking factor for final state electrons and positrons is given by

$$F_{e^{\pm}} = 1 - \frac{1}{\exp((E \pm Q \mp \mu_e)/k_B T) + 1}, \quad (7)$$

where k_B is the Boltzmann constant, $Q \approx 1.293$ MeV is the difference between neutron and proton rest mass energy, μ_e is the electron chemical potential and T is the fluid temperature. The form of $n_{\nu,\tau \lesssim 1}$ for a spherically symmetric heating is

$$n_{\nu,\tau \lesssim 1}(E, R) = \frac{l_{\nu}(E, R)}{4\pi R^2 c \mu_{\nu}(E, R)}, \quad (8)$$

where $l_{\nu}(E, R)$ is the total, spectral number rate (in $\text{s}^{-1}\text{erg}^{-3}$) at radius R obtained as solution of a differential equation that accounts for both emission and absorption of neutrinos while they propagate from the centre of the system to a distance R

$$\frac{dl_{\nu}(E, R)}{dR} = 4\pi R^2 \rho(R) r_{\nu}(E, R) - \frac{\chi_{\text{ab}}(E, R)}{c} H(E, R) l_{\nu}(E, R). \quad (9)$$

In Eq. (8) $\mu_{\nu}(E, R)$ is called flux factor. It corresponds to the average of the cosine of the propagation angle for the free streaming neutrinos. An analytic approximation is given by Liebig et al. (2009)

$$\mu_{\nu}(E, R) = \frac{1}{2} \left(1 + \sqrt{1 - \left(\frac{R_{\nu}(E)}{\max(R, R_{\nu}(E))} \right)^2} \right), \quad (10)$$

where $R_{\nu}(E)$ is the neutrino surface radius for energy E . Far from the neutrino surface ($R \gg R_{\nu}$) the neutrino flux points toward the observer direction and the propagation angle is 0, i.e. $\mu_{\nu}(E, R) = 1$. Close to the neutrino surface ($R \sim R_{\nu}$) and assuming isotropic neutrino emission above the plane tangential to it $\mu_{\nu}(E, R) \sim 1/2$.

Given the spectral, specific rates $r_{\nu}(E, \mathbf{x})$ and $h_{\nu}(E, \mathbf{x})$ at each point from Eqs. (5) and (6), the energy-integrated emission and absorption specific rates are

$$R_{\nu}^k(\mathbf{x}) = \int_0^{+\infty} r_{\nu}(E, \mathbf{x}) E^{2+k} dE, \quad (11)$$

$$H_{\nu}^k(\mathbf{x}) = \int_0^{+\infty} h_{\nu}(E, \mathbf{x}) E^{2+k} dE, \quad (12)$$

respectively, where $k = 0$ specifies the number rate ($\text{g}^{-1}\text{s}^{-1}$) and $k = 1$ the energy rate ($\text{erg g}^{-1}\text{s}^{-1}$). Eqs. (11) and (12) define the specific number and energy net rates $\dot{Q}_{\nu}^{k=0}(\mathbf{x})$ and $\dot{Q}_{\nu}^{k=1}(\mathbf{x})$

$$\dot{Q}_{\nu}^{k=0}(\mathbf{x}) = R_{\nu}^{k=0}(\mathbf{x}) - H_{\nu}^{k=0}(\mathbf{x}), \quad (13)$$

$$\dot{Q}_{\nu}^{k=1}(\mathbf{x}) = R_{\nu}^{k=1}(\mathbf{x}) - H_{\nu}^{k=1}(\mathbf{x}), \quad (14)$$

from which the total neutrino number net rate $L_{\nu}^{k=0}$ and the neutrino luminosity $L_{\nu}^{k=1}$ can be derived by integrating over the volume V of the fluid

$$L_{\nu}^{k=0} = \int_V \dot{Q}_{\nu}^{k=0}(\mathbf{x}) \rho(\mathbf{x}) dV, \quad (15)$$

$$L_{\nu}^{k=1} = \int_V \dot{Q}_{\nu}^{k=1}(\mathbf{x}) \rho(\mathbf{x}) dV. \quad (16)$$

From the last two equations the neutrino average energy is calculated as

$$\langle E_{\nu} \rangle = \frac{L_{\nu}^{k=1}}{L_{\nu}^{k=0}}. \quad (17)$$

The root-mean squared (rms) energy can be defined too as

$$E_{\text{rms}} = \sqrt{\frac{L_{\nu}^{k=2}}{L_{\nu}^{k=0}}}. \quad (18)$$

In Sec (3) we will mainly refer to Eq. (17) to describe the neutrino energy, but we additionally provide values for the rms energies for completeness. From Eqs. (11) and (12) we can also recover the local net change in the total lepton number fraction $\dot{Y}_l(\mathbf{x})$

$$\dot{Y}_l(\mathbf{x}) = m_b (H_{\nu_e}^{k=0}(\mathbf{x}) - H_{\nu_{\bar{e}}}^{k=0}(\mathbf{x}) + R_{\nu_e}^{k=0}(\mathbf{x}) - R_{\nu_{\bar{e}}}^{k=0}(\mathbf{x})) \quad (19)$$

where m_b is the baryon mass, and the change of the total specific matter internal energy $\dot{u}(\mathbf{x})$

$$\begin{aligned} \dot{u}(\mathbf{x}) = & - (R_{\nu_e}^{k=1}(\mathbf{x}) + R_{\nu_e}^{k=1}(\mathbf{x}) + 4R_{\nu_{\mu,\tau}}^{k=1}(\mathbf{x})) + \\ & + (H_{\nu_e}^{k=1}(\mathbf{x}) + H_{\nu_e}^{k=1}(\mathbf{x})). \end{aligned} \quad (20)$$

Both $\dot{Y}_l(\mathbf{x})$ and $\dot{u}(\mathbf{x})$ contain variations in the lepton number fraction and specific internal energy by local emission and absorption of neutrinos and by neutrino diffusion that would dominate in the optically thick regime. Denoting the variation of the number and energy of trapped neutrinos per baryon as $\dot{Y}_\nu(\mathbf{x})$ and $\dot{Z}_\nu(\mathbf{x})$ driven by diffusion, we can recover the change in the electron fraction $\dot{Y}_e(\mathbf{x})$

$$\dot{Y}_e(\mathbf{x}) = \dot{Y}_l(\mathbf{x}) - \dot{Y}_{\nu_e}(\mathbf{x}) + \dot{Y}_{\nu_e}(\mathbf{x}) \quad (21)$$

and the rate of change of the specific internal energy due to local neutrino emission and absorption $\dot{e}(\mathbf{x})$

$$\dot{e}(\mathbf{x}) = \dot{u}(\mathbf{x}) - \frac{1}{m_b} (\dot{Z}_{\nu_e}(\mathbf{x}) + \dot{Z}_{\nu_e}(\mathbf{x}) + 4\dot{Z}_{\nu_{\mu,\tau}}(\mathbf{x})). \quad (22)$$

$\dot{Y}_\nu(\mathbf{x})$ and $\dot{Z}_\nu(\mathbf{x})$ are evaluated at first order in time as

$$\dot{Y}_\nu(\mathbf{x}) = \frac{Y_{\nu,t+\Delta t}(\mathbf{x}) - Y_\nu(\mathbf{x})}{\Delta t}, \quad (23)$$

$$\dot{Z}_\nu(\mathbf{x}) = \frac{Z_{\nu,t+\Delta t}(\mathbf{x}) - Z_\nu(\mathbf{x})}{\Delta t}, \quad (24)$$

where Δt is the current time step. An adequate time step should ensure that the variation of all the variables for which the ASL provide a source term in the hydrodynamic equations is less than a given, small percentage (namely $\lesssim 1\%$). The number and energy of trapped neutrinos per baryon at time t and location \mathbf{x} are related to the neutrino-trapped distribution function $f_{\nu,t}^{\text{tr}}(E, \mathbf{x})$ by

$$Y_{\nu,t}(\mathbf{x}) = \frac{4\pi}{(hc)^3} \frac{m_b}{\rho(\mathbf{x})} \int f_{\nu,t}^{\text{tr}}(E, \mathbf{x}) E^2 dE, \quad (25)$$

$$Z_{\nu,t}(\mathbf{x}) = \frac{4\pi}{(hc)^3} \frac{m_b}{\rho(\mathbf{x})} \int f_{\nu,t}^{\text{tr}}(E, \mathbf{x}) E^3 dE, \quad (26)$$

where h is the Planck constant. Starting from $Y_{\nu,t}(\mathbf{x})$ and $Z_{\nu,t}(\mathbf{x})$, $f_{\nu,t}^{\text{tr}}(E, \mathbf{x})$ is first recovered on the basis of equilibrium arguments. In particular, we assume a distribution of the form

$$f_{\nu}^{\text{tr}}(E, \mathbf{x}) = f_{\nu}^{\text{eq}}(E, \mathbf{x}) (1 - e^{-\tau_{\nu,\text{en}}(E, \mathbf{x})}), \quad (27)$$

at time t , where $f_{\nu}^{\text{eq}}(E, \mathbf{x})$ is a Fermi-Dirac distribution

$$f_{\nu}^{\text{eq}}(E, \mathbf{x}) = \frac{1}{e^{(E/(k_B T_\nu(\mathbf{x})) - \eta_\nu(\mathbf{x}))} + 1}, \quad (28)$$

with $T_\nu(\mathbf{x})$ being the neutrino temperature, which is assumed to be equal to the matter temperature, and $\eta_\nu(\mathbf{x})$ the degeneracy parameter, evaluated by assuming weak equilibrium. Second, $f_{\nu,t}^{\text{tr}}(E, \mathbf{x})$ is evolved between t and $t + \Delta t$ considering production and diffusion of neutrinos as two competing processes. Namely, we integrate the equation

$$\frac{df_{\nu}^{\text{tr}}}{dt} = \dot{f}_{\nu,\text{prod}}^{\text{tr}} + \dot{f}_{\nu,\text{diff}}^{\text{tr}}, \quad (29)$$

where

$$\dot{f}_{\nu,\text{prod}}^{\text{tr}} = \frac{f_{\nu}^{\text{eq}} - f_{\nu}^{\text{tr}}}{\max(t_{\nu,\text{prod}}, \Delta t)} \exp\left(-\frac{t_{\nu,\text{prod}}}{t_{\nu,\text{diff}}}\right) \quad (30)$$

and

$$\dot{f}_{\nu,\text{diff}}^{\text{tr}} = -\frac{f_{\nu}^{\text{tr}}}{\max(t_{\nu,\text{diff}}, \Delta t)} \exp\left(-\frac{t_{\nu,\text{diff}}}{t_{\nu,\text{prod}}}\right). \quad (31)$$

At last, $Y_{\nu,t+\Delta t}$ and $Z_{\nu,t+\Delta t}$ are recovered by using $f_{\nu,t+\Delta t}^{\text{tr}}$ in Eqs. (25) and (26). For more details, see [Perego et al. \(2016\)](#). Note that in Eqs. (19) and (20) we have neglected absorption by heavy-lepton neutrinos in the semi-transparent regime, because at the decoupling surfaces they do not have enough energy to produce muons and taus by charged-current interactions. Moreover, heating by heavy-lepton neutrino annihilation and inverse nucleon-nucleon bremsstrahlung provides negligible contributions in the semi-transparent regime, since the opacities are small ([Endrizzi et al. 2019](#)). Neglecting heating by heavy-lepton neutrinos is therefore a reasonable assumption.

2.2 Multi-D implementation

All physical quantities shown in Sec. 2.1 are local and independent of the system geometry, except for Eqs. (1),(8) and (10). In particular, Eq. (10) is straightforward to use only in cases where the neutrino surface is easy to reconstruct. While this argument is certainly valid for a spherically symmetric configuration, for a more complex geometry like a neutron star merger remnant is not. Indeed, given the presence of a torus around the central compact object the neutrino decoupling surface has larger radii on the equatorial plane than along the polar axis ([Dessart et al. 2009](#); [Perego et al. 2014](#)). In the following, we describe our implementation of Eqs. (1),(8) and (10) to a multi-D configuration.

2.2.1 Optical depth

The computation of the optical depth is performed by taking the minimum among values of the optical depth calculated by integrating the neutrino mean free path over a set of pre-defined radii. In particular, given a point (x,y,z) we consider the following outgoing paths:

- fixed (y,z) , path along x
- fixed (x,z) , path along y
- fixed (x,y) , path along z
- fixed x , diagonal path along y,z
- fixed y , diagonal path along x,z
- fixed z , diagonal path along x,y
- diagonal path along x,y,z .

The likelihood of being close to the true minimum optical depth at a point increases by increasing number of paths. For this reason, the choice of diagonal paths ensures a more accurate calculation of the optical depth by avoiding local overestimates that would arise otherwise. However, it is important to stress that this algorithm leads inevitably to an overestimation of the local optical depth, as a consequence of the limited number of paths that can be practically chosen for calculations.

2.2.2 Flux factor

To construct a more general form for the flux factor that still resembles the general properties of Eq. (10) we borrow

the linear dependence of the inverse flux factor from the optical depth from equation (31) of O'Connor & Ott (2010). Although their equation (31) does not consider a spectral distribution of energies, we take that form to get an approximate expression of the flux factor at any energy by just extending the grey interpolation formula to a spectral form by adding the energy dependence. Therefore, we use

$$\frac{1}{\mu_\nu}(E, \mathbf{x}) = \begin{cases} 1.5 \tau_{\nu, \text{tot}}(E, \mathbf{x}) + 1 & \text{if } \tau_{\nu, \text{tot}}(E, \mathbf{x}) \leq 2/3 \\ 2 & \text{otherwise} \end{cases}. \quad (32)$$

Using this expression we mimic Eq. (10) with a flux factor $\mu_\nu(E, \mathbf{x})$ tending to 1 for small optical depths and having its minimum value at $\tau_{\nu, \text{tot}}(E, \mathbf{x}) = 2/3$ equal to $1/2$. Moreover, we enforce a similar constraint as in Eq. (6) by setting the value of the flux factor to be $1/2$ for any optical depth larger than $2/3$. Eq. (32) is more suitable than Eq. (10) for a general geometry since it only depends on the local optical depth, and no previous knowledge of the radius of the neutrino surface is required. However, a different choice of the flux factor might lead to noticeable variations of the amount of heating. We will quantify the effects of this choice of flux factor in the next section.

2.2.3 Flux anisotropy

Modelling the neutrino density distribution in space accurately requires the knowledge of the path along which neutrinos propagate from the optically thick to the optically thin region. While this is trivial in spherical symmetry, it is not so for a general geometry such as a merger remnant. Sophisticated algorithms have been designed (Perego et al. 2014), but come at large computational expense. Here we take a simpler approach. We modify Eq. (8) according to the equation (3) of Martin et al. (2018). In their work the total, axially symmetric neutrino flux an observer receives far from the neutrino emitting region is approximated by

$$J_\nu(\theta, R) = \frac{3(1 + \beta_\nu \cos^2 \theta)}{3 + \beta_\nu} \frac{L_\nu^{k=1}(\theta, R)}{4\pi R^2 \langle E_\nu \rangle}, \quad (33)$$

where θ is the angle of the observer with respect to the source pole and $\beta_\nu = \frac{J_\nu(\theta=0, R)}{J_\nu(\theta=\pi/2, R)} - 1$ measures the degree of flux anisotropy which depends on the geometry of the source. In particular, a spherically symmetric source would have $\beta_\nu = 0$. On the other hand, in the context of mergers the presence of a torus implies more escaping neutrinos along the polar region rather than along the optically thick equatorial region, and therefore $\beta_\nu > 0$ (Rosswog & Liebendörfer 2003; Dessart et al. 2009; Perego et al. 2014; Foucart et al. 2016). In order to adapt Eq. (33) to our problem of reconstructing the neutrino density distribution in our domain, we assume a similar modulation $\sim \cos^b(\theta)$, but we gauge the exponent b by comparison with an M1 neutrino transport approach. Moreover, we make the assumption that the value of β_ν that would in principle be a function of the distance to the source of neutrino emission is constant and equal to the value measured at large distances. Furthermore, at distances close to the neutrino surface the effects of the neutrino angular distribution arise and the hypothesis of pure radial fluxes breaks down. We thus calculate the neutrino density $n_{\nu, \tau \lesssim 1}(E, \mathbf{x})$ at each radius $R = |\mathbf{x}|$ as in Eq. (8) by retaining a spherically symmetric neutrino spectral number rate

$l_\nu(E, |\mathbf{x}|)$, but on one side we add the flux factor $\mu_\nu(E, \mathbf{x})$ of Eq. (32) and on the other side we include the modulation factor $\sim \cos^b(\theta)$ to keep track of the effect of the geometry of the system on the neutrino fluxes. Therefore we replace Eq. (8) with

$$n_{\nu, \tau \lesssim 1}(E, \mathbf{x}) = \frac{(1+b)(1+\beta_\nu \cos^b(\theta))}{1+b+\beta_\nu} \frac{l_\nu(E, |\mathbf{x}|)}{4\pi |\mathbf{x}|^2 c \mu_\nu(E, \mathbf{x})}, \quad (34)$$

where $\theta \equiv \theta(\mathbf{x})$ and we rewrite the angular dependent prefactor such that the integral over the solid angle is 4π . Note that unlike Eq. (10) we use $\mu_\nu(E, \mathbf{x})$ from Eq. (32) and therefore points in space at same distance $R = |\mathbf{x}|$ to the centre of the system can potentially have different values of the flux factor. Only for spherically symmetric systems they are the same and we recover Eq. (8) by setting $\beta_\nu = 0$. Note that in Eq. (8) we keep the assumption of axial symmetry when calculating the flux modulation. A high degree of axisymmetry is generally expected after few tens of ms irrespective of the mass ratio (Perego et al. 2019). This timescale reduces even more if angular momentum transport by turbulent magnetic viscosity is effective. Therefore, except the first few ms after the merger, our assumption of axis symmetry is reasonable. As last step we estimate β_ν considering an approach similar to the one of Rosswog & Liebendörfer (2003). We divide neutrinos in two groups: diffusive and free streaming neutrinos. The former propagate outward following the direction of the gradient $\hat{n}_\rho = -\nabla \rho / |\nabla \rho|$, while the latter are emitted isotropically. The luminosity at a polar angle θ coming from the diffusive neutrinos is selected by choosing those neutrinos emitted within a ring of width $\Delta\theta$ around the θ direction. Therefore, the luminosity per solid angle $\Lambda_\nu(\theta) = \frac{\Delta L_\nu^{k=1}}{\Delta\Omega}$ is

$$\Lambda_\nu(\theta) = \frac{\sum_i R_{i,\nu,\text{diff}}^{k=1}(\theta) m_i}{2\pi \sin(\theta) \Delta\theta} + \frac{\sum_j R_{j,\nu,\text{prod}}^{k=1} m_j}{4\pi}, \quad (35)$$

where the index i in the sum is limited to those fluid points for which $\theta - \Delta\theta/2 < \theta_i < \theta + \Delta\theta/2$ and $\cos(\theta_i) = \hat{n}_\rho \cdot \hat{e}_z$, \hat{e}_z being the unit vector along the z-axis, and the index j extends over the whole volume. m_i and m_j are the masses of the fluid elements i and j . The diffusive and free streaming contributions to the luminosity are calculated as

$$R_{i,\nu,\text{diff}}^{k=1}(\theta) = \int_0^{+\infty} f_{i,\nu,\text{diff}}(E) r_{i,\nu}(E) E^3 dE \quad (36)$$

$$R_{j,\nu,\text{prod}}^{k=1} = \int_0^{+\infty} f_{j,\nu,\text{prod}}(E) r_{j,\nu}(E) E^3 dE \quad (37)$$

with $f_{i,\nu,\text{diff}}(E)$ and $f_{j,\nu,\text{prod}}(E)$ being the fractions of diffusive and free streaming contribution to the emission rates $r_{i,\nu}(E)$ and $r_{j,\nu}(E)$ at i and j points respectively, which can be approximated by ³

$$f_{i,\nu,\text{diff}}(E) \approx \frac{\tilde{r}_{i,\nu}(E)}{r_{i,\nu,\text{diff}}(E)}, \quad (38)$$

$$f_{j,\nu,\text{prod}}(E) \approx \frac{\tilde{r}_{j,\nu}(E)}{r_{j,\nu,\text{prod}}(E)}. \quad (39)$$

³ We neglect the Pauli blocking and the thermalization correction for this calculation.

The value of β_ν is then estimated from the ratio of the fluxes $\sim \frac{\Lambda_\nu}{R^2}$ an observer close to pole and equator would see at a fixed distance R to the source ⁴

$$\beta_\nu = \frac{\Lambda_\nu(\theta \approx 0^\circ)}{\Lambda_\nu(\theta \approx 90^\circ)} - 1. \quad (40)$$

It is important to note that in the computation of β_ν we distinguish between neutrino species as the relevant neutrino-matter interactions differ between them and they also have different decoupling surfaces (see Figure 11 for example), but for each species we do not consider different β_ν for different neutrino energies. Nevertheless, our algorithm accounts for the different contributions to β_ν from different energies and therefore we assume Eq. (40) as indicative for a suitable estimate of the spectral neutrino density of Eq. (34).

3 RESULTS

In this section we summarise our results. We begin by applying the ASL to a 1D core-collapse supernova profile. Subsequently we map this profile on a 3D grid and apply our multi-D implementation of the ASL, see Sec. 2.2. Finally, we use the ASL to extract the neutrino physics from a neutron star merger remnant. Our tests are performed by taking snapshots of density, temperature and electron fraction from dynamical simulations (Rosswog et al. 2017) as a background on which we evolve the neutrino quantities until they achieve a steady state. For the core collapse supernovae tests, we use the Lattimer-Swesty Equation of State (EoS) (Lattimer & Douglas Swesty 1991) with nuclear incompressibility $K = 220$ MeV, a standard choice widely used throughout the literature. In light of the recent constraints on the EoS from gravitational and electromagnetic observations of GW170817 (Coughlin et al. 2018; Radice et al. 2018a; Most et al. 2018; Abbott et al. 2018) for the binary merger remnant we consider the SFHo EoS, which provides masses in agreement with the highest neutron star masses measured until very recently (Demorest et al. 2010; Antoniadis et al. 2013), but in tension with the most recent measurement of a $2.17^{+0.11}_{-0.10} M_\odot$ neutron star (Cromartie et al. 2019). The neutrino transport is run with a spectrum of 20 geometrically increasing energy groups from 3 MeV to 300 MeV. We also explore for fixed energy interval the convergence of our results by changing the number of energy bins, and for fixed number of bins we also increase and decrease the energy interval to test the dependence of our results on the energy spectrum. Our ASL results are compared with a two moment scheme (M1) (Thorne 1981). In particular, for the core-collapse supernovae tests we compare with the M1 scheme of the spherically symmetric Eulerian hydrodynamics code GR1D (O'Connor & Ott 2010; O'Connor 2015; O'Connor & Ott 2013). Since we take the 1D core-collapse supernova snapshot from the dynamical simulations of Perego et al.

(2016), which uses the same ASL described in Sec. 2.1, we perform a dynamical simulation of the same progenitor with GR1D and take the outcome from the simulation at the same time post-bounce to make a consistent comparison. For the binary neutron star merger case we compare with the M1 scheme implemented in the Eulerian hydrodynamics code FLASH (Fryxell et al. 2000; O'Connor & Couch 2018). Unlike the core-collapse case, we take a snapshot of a post-merger remnant from the simulations of Rosswog & Liebendörfer (2003), which uses a grey leakage scheme, and apply both the ASL implementation described in Sec. 2.2 and the M1 scheme in FLASH to it. Applying a different transport approach to the one adopted for obtaining the snapshot introduces inconsistencies that will be quantified.

3.1 ASL in 1D core-collapse supernovae

We take a snapshot at 275 ms post-bounce of the $15 M_\odot$ progenitor of Perego et al. (2016), whose dynamical evolution has been simulated with the spherically symmetric hydrodynamics code *Agile* (Liebendörfer et al. 2002). The radial profile has a variable resolution with radius ranging from $\lesssim 1$ km to tens of km moving from the inner to the outer regions, with a maximum radial extension of 6832 km. In order to describe the profile properties, it is worth summarising the previous dynamics. During the collapse phase the deleptonization of the iron core reduces the fraction of electrons Y_e in the core by producing electron neutrinos. Neutrinos freely stream out initially and therefore the total lepton number decreases. Once neutrinos get trapped, the decrease in Y_e is compensated by the fraction of trapped neutrinos. At core bounce a shock forms and propagates outward. During the shock propagation, iron nuclei falling into the shock are photo-dissociated into neutrons and protons. At this stage, neutrinos of all flavours are largely produced by charged current interactions and pair processes. Dissociation of iron nuclei into nucleons, the ram pressure of the still infalling outer layers, and the energy losses due to the neutrino burst when it surpasses the neutrinosphere, cause the shock to stall. Neutrino absorption behind the shock in the so called gain region helps the shock to revive and in some cases leads to the final explosion. In the top row panels of Figure 1 we show density, temperature and electron fraction as a function of the radius, while in the second and third rows we show the number and energy of trapped neutrinos per baryon, denoted as Y_ν and Z_ν respectively.

We evolve such fractions until steady state is reached while keeping density, temperature and electron fraction of the fluid fixed. Once in equilibrium, the rates of the trapped neutrino components vanish, which translates into $\dot{u} = \dot{e}$ and $\dot{Y}_l = \dot{Y}_e$, see Eqs. (20) and (21). The distribution of \dot{u} and \dot{Y}_l (from a simulation using the flux factor of Eq. (32)) is shown in Figure 2. All the results we are going to show are referred to this equilibrium state.

3.1.1 Neutrino rates

In Figure 3 we show the specific emission rate along the radial profile for different energies, obtained from Eq. (5) by multiplying for each energy by $E^2 \Delta E$ of the corresponding bin, as well as the cumulative contribution from all energies.

⁴ We do not exactly choose the angles $\theta = 0^\circ$ and $\theta = 90^\circ$ for two reasons: first, the solid angle corresponding to $\theta = 0^\circ$ is small and the value of $\Lambda_\nu(\theta = 0^\circ)$ would be associated to a small region that would not be representative of the flux at the pole. Second, the cosine dependence is only meant as an approximate trend of the flux between pole and equator. We therefore set our fiducial angles close to pole and equator to $\theta = 10^\circ$ and $\theta = 80^\circ$ respectively.

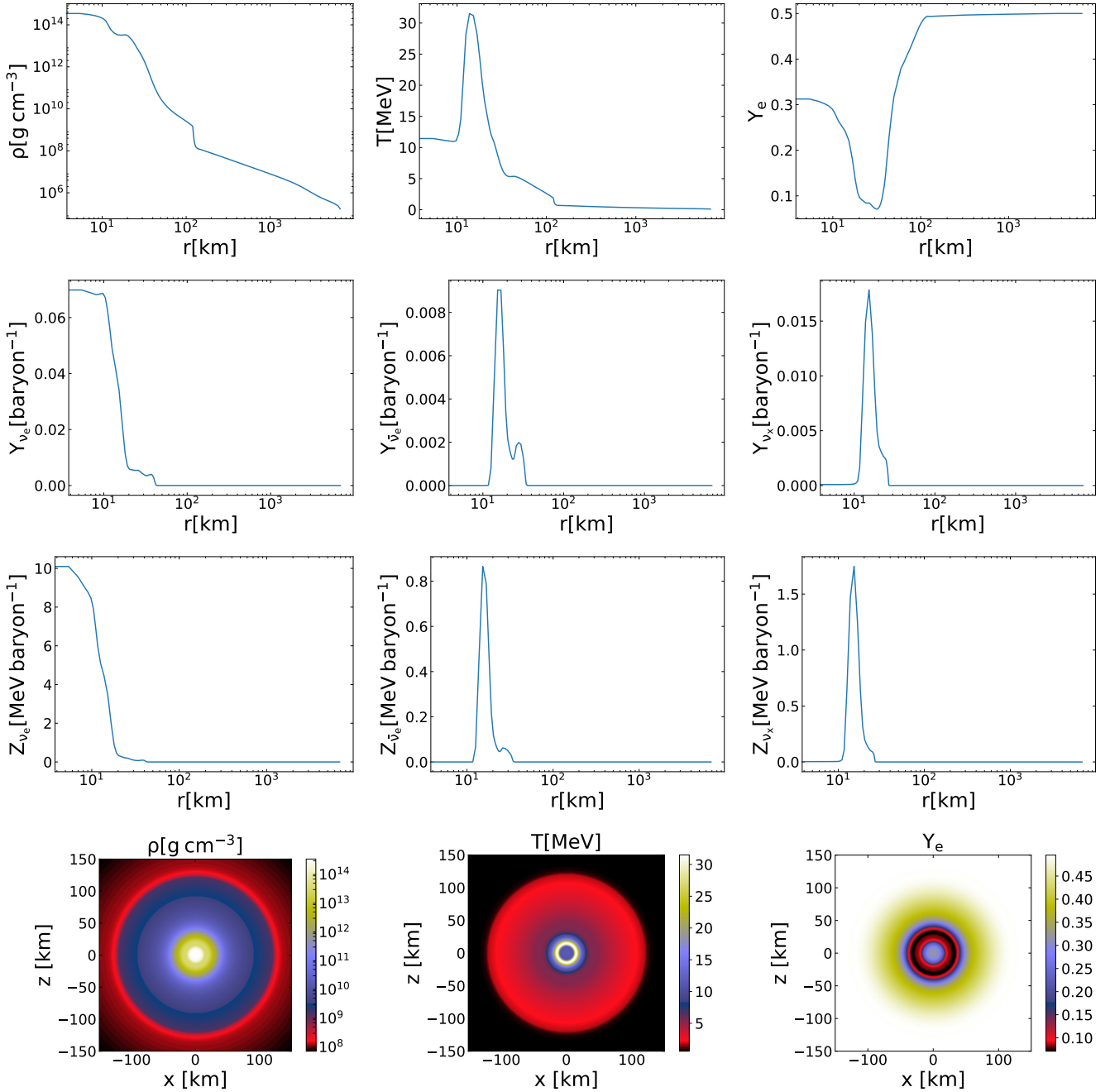


Figure 1. **Top row:** 1D profile of density (left panel), temperature (middle panel) and electron fraction (right panel) at 275 ms after core bounce. The shock is located at ~ 120 km from the core, clearly visible from the jump of density and temperature. Their values in the core are about $\rho \sim 3 \cdot 10^{14}$ g cm $^{-3}$ and $T \sim 12$ MeV respectively. The effect of the deleptonization until neutrino trapping leads to a inner electron fraction of $Y_e \sim 0.3$. The passage of the shock during its propagation affects both T and Y_e sensitively. In particular, neutrino-matter interactions after iron nuclei dissociation decrease the electron fraction down to $Y_e \sim 0.1$. Conversely, temperatures reach their maximum at $T \sim 30$ MeV. Matter properties in the outermost layers are untouched by the shock and therefore have their original Y_e and low values of T . **Second and third rows:** number and energy of trapped neutrinos per baryon along the 1D profile. From left to right, electron neutrinos, electron anti-neutrinos and heavy-lepton neutrinos. Electron neutrinos are confined within a region of ~ 20 km from the core, while electron anti-neutrinos and heavy-lepton neutrinos are within $10 - 30$ km. **Bottom row:** density (left panel), temperature (middle panel) and electron fraction (right panel) of the core-collapse snapshot at 275 ms after bounce on the $y=0$ plane of the 3D grid. The peak in the temperature that is visible at $T \sim 20$ km in the 1D profile is shown here in yellow. In the same way, the drop in the electron fraction down to $Y_e \sim 0.1$ corresponds to the black-red region.

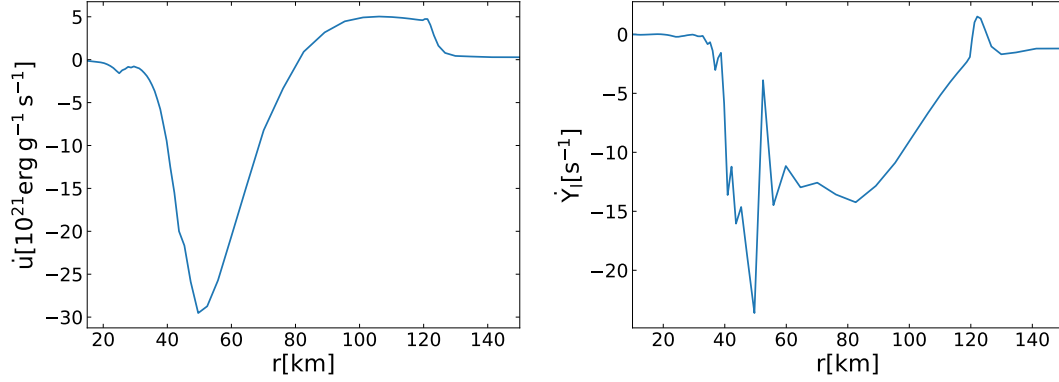


Figure 2. Specific total internal energy rate (left panel) and lepton number fraction rate (right panel) once steady state is reached. Negative values of \dot{u} describe the loss of internal energy due to neutrino emission at equilibrium, while positive values mark the region where the heating dominates. The negative electron fraction rate is a result of the conversion of electrons into neutrinos.

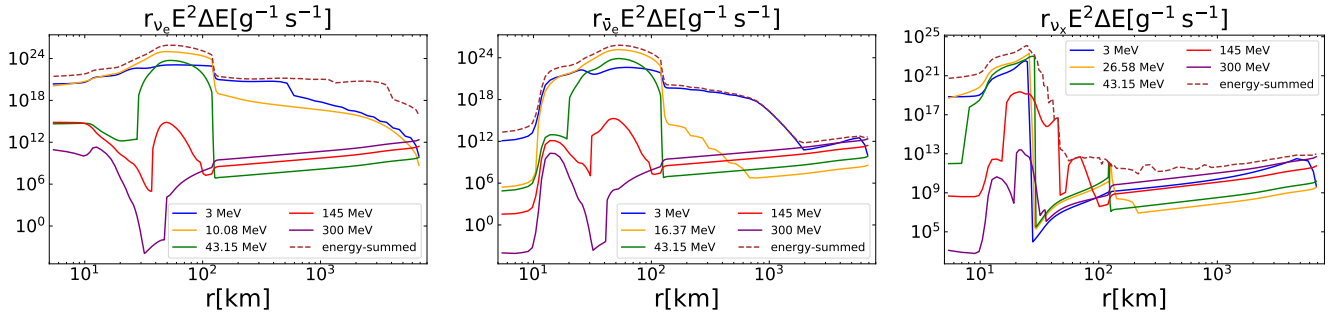


Figure 3. Specific emission rate at different energies between 3 MeV to 300 MeV for electron neutrinos (left panel), electron anti-neutrinos (middle panel) and heavy-lepton neutrinos (right panel). The dashed-line corresponds to the energy-summed rate. In contrast to electron neutrinos and anti-neutrinos, heavy-lepton neutrinos can still provide an important contribution to the emission at energies $\gtrsim 40$ MeV. Low-energy neutrinos contribute the most to the local emission.

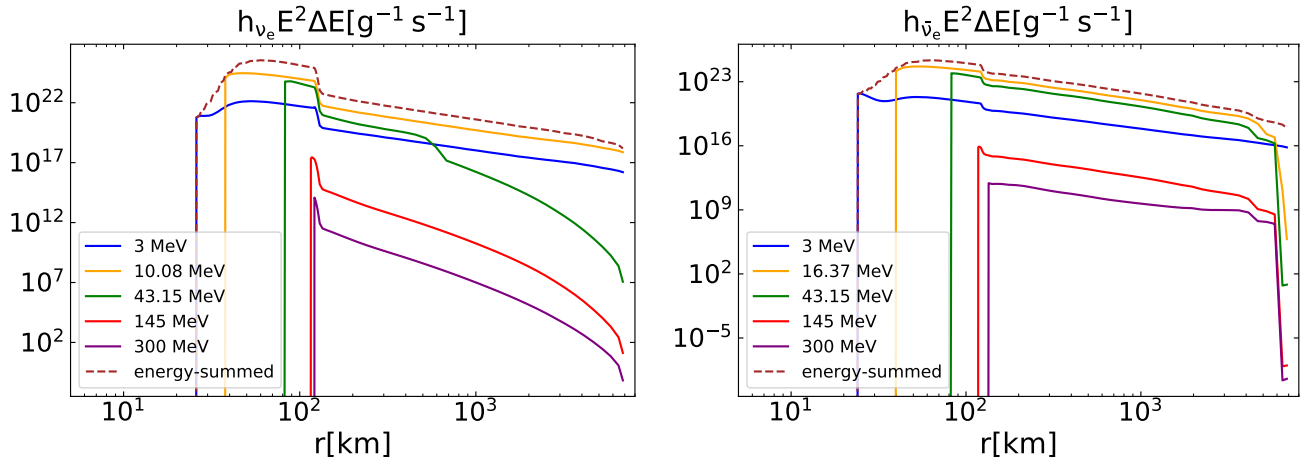


Figure 4. Specific absorption rate at different energies between 3 MeV to 300 MeV for electron neutrinos (left panel) and electron anti-neutrinos (right panel). The dashed-line corresponds to the energy-summed rate. The largest contribution to the local absorption is provided by low energy neutrinos.

The main contribution to the neutrino emission comes from neutrino energies below \sim few tens of MeV for all neutrino species. In particular, all species show a decreasing contribution to the emission with increasing energy at low radii because of the $\sim \tau_{\nu, \text{tot}}^{-2} \sim E_{\nu}^{-2}$ dependence of the diffusion rate (equation (31) of Perego et al. (2016)) that causes high energy neutrinos to have a lower diffusion rate and therefore to diffuse out less efficiently than low energy neutrinos. The production rate dominates over the diffusion rate at large radii. Given the emissivity dependence $\sim j_{\nu}$ (equation (30) of Perego et al. (2016)), neutrino emission is governed by the low temperatures and is therefore suppressed at all energies. Similarly, in Figure 4 we show the specific absorption rate for electron neutrinos and anti-neutrinos (heavy-lepton neutrinos are not included in the heating). Neutrino absorption is calculated locally for each neutrino energy if the condition $\tau_{\text{en}, \nu}(E, \mathbf{x}) \leq 1$ is satisfied, and depends on the local amount of available neutrinos, which in turn depends on both local production and on neutrinos coming from innermost regions. Local neutrino production decreases as the radius increases, as a consequence of the decrease in temperature and density. In addition, the amount of neutrinos at a given radius coming from innermost regions is reduced both by absorption occurring at smaller radii and by the $\sim 1/R^2$ dependence in Eq. (34). Therefore, all energies show a decrease in the local neutrino absorption with increasing distance from the centre. We also notice in the same way of the emission rate that the larger contribution to the heating rate comes from neutrinos of \sim few tens of MeV, as a result of the dependence of the neutrino absorption on the emission via the number rate $l_{\nu}(E, \mathbf{x})$.

3.1.2 Flux factor and heating

In Figure 5 we compare the inverse of the flux factor for the two prescriptions of Eqs. (10) and (32), labelled as *old* and *new* respectively, for electron neutrinos and anti-neutrinos at different energies, as it enters Eq. (6) and it therefore affects the local heating. The largest differences are at energies $\gtrsim 40$ MeV with discrepancies up to $\sim 25 - 30\%$. Such differences are expected since the flux factor from Eq. (32) depends on the optical depth rather than the radius as in Eq. (10), and therefore the trend in Figure 5 resembles the trend of the optical depth. Nevertheless, as we have seen in Figure 4 the largest contribution to the heating comes from neutrinos of energies of few tens of MeV. We therefore do not expect such differences to contribute sensitively to the global neutrino luminosities for our snapshot calculations. In fact, in the bottom panels of Figure 6 we show the quantity $-\dot{Q}_{\nu}^{k=1}$ in units of $10^{20} \text{ erg g}^{-1} \text{ s}^{-1}$ calculated from Eq. (14), which is a measure of the local heating rate. Overall, we see a very good agreement between the old (blue line) and new (red line) flux factor prescriptions, with differences at the order of a few percent in the region where heating gets important ($-\dot{Q}_{\nu}^{k=1} > 0$). More detailed quantification of the heating with our new flux factor prescription during full dynamical simulations will be the subject of future work.

As an additional test, we show in Figure 6 a comparison at the same time post-bounce of the same quantity $-\dot{Q}_{\nu}^{k=1}$ provided by a dynamical evolution of the same progenitor starting at the onset of collapse performed with GR1D (black-dashed line). Compared to our test with the ASL, the net

rate from GR1D provides less cooling (less negative $-\dot{Q}_{\nu}^{k=1}$) in the ranges $\sim 30 - 50$ km and $\sim 65 - 80$ km, with a larger one only in the range $\sim 50 - 65$ km for electron neutrinos. This is the result of a dynamical evolution with a different neutrino transport, where at the same time after bounce the structure of the star shows significant differences with respect to the ASL run, clearly visible in the density and temperature profiles on the top panels of Figure 6. In particular, the GR1D profile has a colder and less compact layer within $\sim 30 - 50$ km where most of the emission occurs. Note also the different location of the shock, which is located at ~ 105 km for the GR1D case. On the other hand, we do not see a difference in the peak heating rate near 100 km, with $-\dot{Q}_{\nu}^{k=1} \sim 2.5 \cdot 10^{20} \text{ erg g}^{-1} \text{ s}^{-1}$ for both runs.

3.1.3 Neutrino luminosities and average-rms energies

Given the specific net rates we calculate the total neutrino luminosities and average energies given by Eqs. (16) and (17). The results are shown in the first row of Table 1 for both the old and the new flux factor prescriptions. The latter reduces the luminosities compared to the former by $\lesssim 5\%$. The average energies are less affected with differences $\lesssim 1\%$. For completeness, we also calculate the rms neutrino energies from Eq. (18) and find $E_{\text{rms}, \nu_e} = 14.21$ MeV, $E_{\text{rms}, \bar{\nu}_e} = 17.07$ MeV, $E_{\text{rms}, \nu_{\mu}} = 25.33$ MeV, in agreement with Perego et al. (2016). We further show the results obtained by performing the same calculations with GR1D in the last row of Table 1. The electron neutrino and anti-neutrino luminosities are lower by $\lesssim 10\%$ compared to the ASL runs due to the combination of an overall weaker neutrino cooling and comparable heating. Heavy lepton neutrinos have instead $\sim 7\%$ lower luminosity. By looking at the average energies, differences are at the level of $\lesssim 5\%$ for electron neutrinos and anti-neutrinos, and of $\sim 7\%$ for heavy-lepton neutrinos. A similar trend is seen in the rms energies. Overall, beside the different grid setups, these discrepancies are a consequence of the usage of different neutrino transport schemes.

3.1.4 Number of energy bins

We finally determine the number of energy bins that are needed for trustworthy results for the luminosities and average energies. We first vary the number of energy bins in the fixed energy interval $[3, 300]$ MeV. Table 2 summarises our findings. A number of energy bins $\lesssim 10$ causes sensitive deviation from a regime of convergence that is visible at larger numbers (which includes our preliminary choice of 20 energy groups in $[3, 300]$ MeV). In particular, we notice a decrease in the luminosities and to a minor extent in the average energies, as a result of poorly resolved energy-integrated emission and absorption rates. We therefore choose 20 energy bins and vary the energy interval. In this way, variations in the simulation outcome by a reduction of the spectrum size would provide information on those energy ranges that are too small regardless of the number of energy bins. Moreover, we can assess whether the regime of convergence with 20 bins is satisfied for wider intervals of energies or if it is strictly bound to certain energy ranges. Results are shown in Table 3. We see that cutting the energy spectrum $[3, 300]$ MeV at high energies leads to a significant decrease

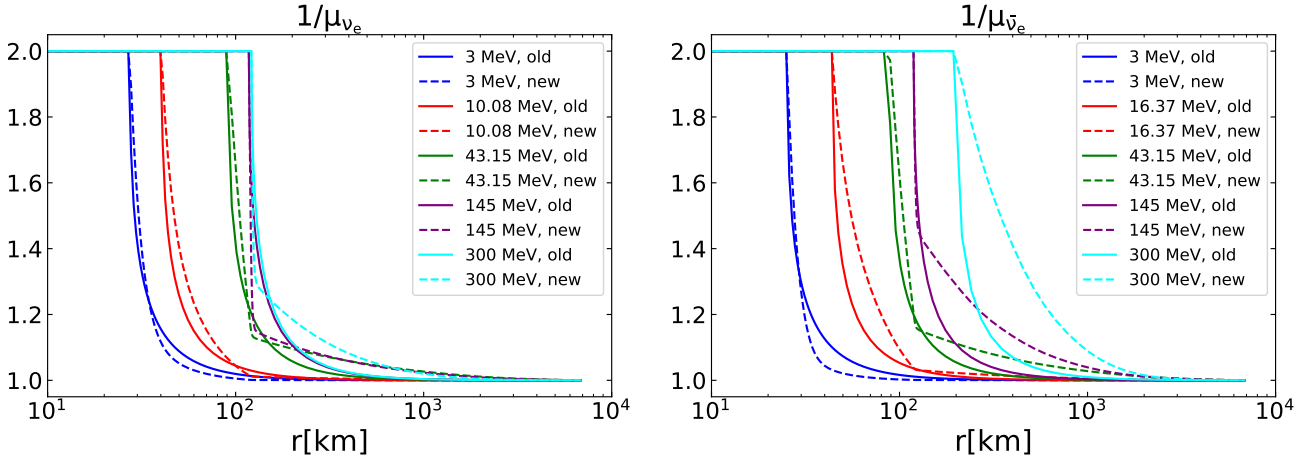


Figure 5. Inverse of the electron neutrino (left panel) and anti-neutrino (right panel) flux factor for the prescriptions of Eqs. (10) and (32), labelled as *old* and *new* respectively. Different neutrino energies of the global spectrum are chosen as reference. Note the larger deviations from the old prescription at high energies, due to the τ -dependence of the new prescription.

of $L_{\nu_x}^1$ that starts appearing from spectra with upper energies below ~ 75 MeV and that worsen by up to about 50% decrease for the smallest range [3, 30] MeV. The average energy $\langle E_{\nu_x} \rangle$ is also reduced to 14.37 MeV. This reduction is due to the lack of contribution coming from energies $\gtrsim 40$ MeV, that can still be relevant to the emission from heavy-leptons (see left panel of Figure 3). In contrast, electron neutrino and anti-neutrino values remain almost stationary. In the same way, cutting the energy spectrum at low energies from 3 MeV has a strong impact on the luminosities, with a reduction of up to 70 – 80% for electron neutrinos and anti-neutrinos in the case of the [25, 300] MeV range. The average energies show the opposite trend, increasing as a result of the high energies giving contribution to the luminosity L_{ν}^1 via Eqs. (11), (12) and (14) and thus affecting the mean of Eq. (17). On the other hand, we notice a convergence in the values of L_{ν}^1 and $\langle E_{\nu} \rangle$ for spectra spanning a range from 3 MeV to hundreds of MeV. In particular, no sensitive variations are seen by extending the interval of energies above 300 MeV. The smallest interval above which we start seeing convergence is [3, 75] MeV. However, it is important to specify that we are here basing our convergence tests by just looking at global neutrino luminosities and neglecting the convergence of the fractions of neutrinos trapped components Y_{ν} and Z_{ν} which are crucial in the modelling of the diffusion while performing dynamical simulations. Such convergence requires neutrinos of energies at least equal to the neutrino chemical potential in the core (set by the beta-equilibrium condition), i.e. $\gtrsim 100$ MeV. Moreover, we want to stress that our convergence tests are performed over a snapshot, but the way the selected energy interval affects the emission can change for different stages of a dynamical evolution. Summarising, a number of 20 energy bins for the neutrino spectrum is a reasonable choice despite the assumed interval of energies, provided that there are neither cuts in the spectrum at low energies nor at energies that would exclude neutrinos of $\gtrsim 100$ MeV.

3.2 ASL in 3D applications

3.2.1 Comparison in spherical symmetry between 1D and 3D

To scrutinise our multi-D implementation, we start by taking the snapshot analyzed in Sec. 3.1, map the initial data on a 3D grid with uniform resolution of 1 km and evolve the neutrino transport part until equilibrium. Instead of mapping the whole radial profile which extends up to 6832 km at densities below 10^6 g/cm³ and temperatures of ~ 0.1 MeV, we take the profile information only up to 150 km and neglect the remaining part to save computational time. Indeed, beyond such distances densities and temperatures are low enough that the neutrino contribution to the outcome of the simulations is negligible, $\lesssim 1\%$ in the total luminosities and average energies. We choose the energy interval [3, 300] MeV, see Sec. 3.1. We show the mapped initial conditions on the $y=0$ plane in the bottom panel of Figure 1.

3D optical depth

To test our 3D implementation of the optical depths, we first calculate the optical depth on the 3D grid as explained in Sec. 2.2. We then create a 1D profile equivalent to the one used in Sec. 3.1 but with uniform resolution of 1 km, where we calculate the optical depth by doing a simple integration over the radial path. We finally map such optical depth on the 3D grid and calculate the relative error $\varepsilon_{\nu} = \frac{\tau_{1D} - \tau_{3D}}{\tau_{1D}}$ on the $y=0$ plane. In the left panel of Figure 7 we show our result. As reference case we take the total optical depth for electron neutrinos of energy $E_{\nu_e} = 10.08$ MeV, the other energies and neutrino species show a similar behaviour. The differences between the 1D and the 3D calculations are at the level of $\sim 8\%$ at the most, with the 3D implementation providing larger values overall. To get an idea of the distribution of the neutrino surfaces at different energies, we show the location of the total and energy neutrinosphere radii on the density map at $y=0$ in Figure 8. The selected set of energies are the same used to show the plots in Figures 3 and 4. The neutrino surfaces are almost perfectly spherical, suggesting that

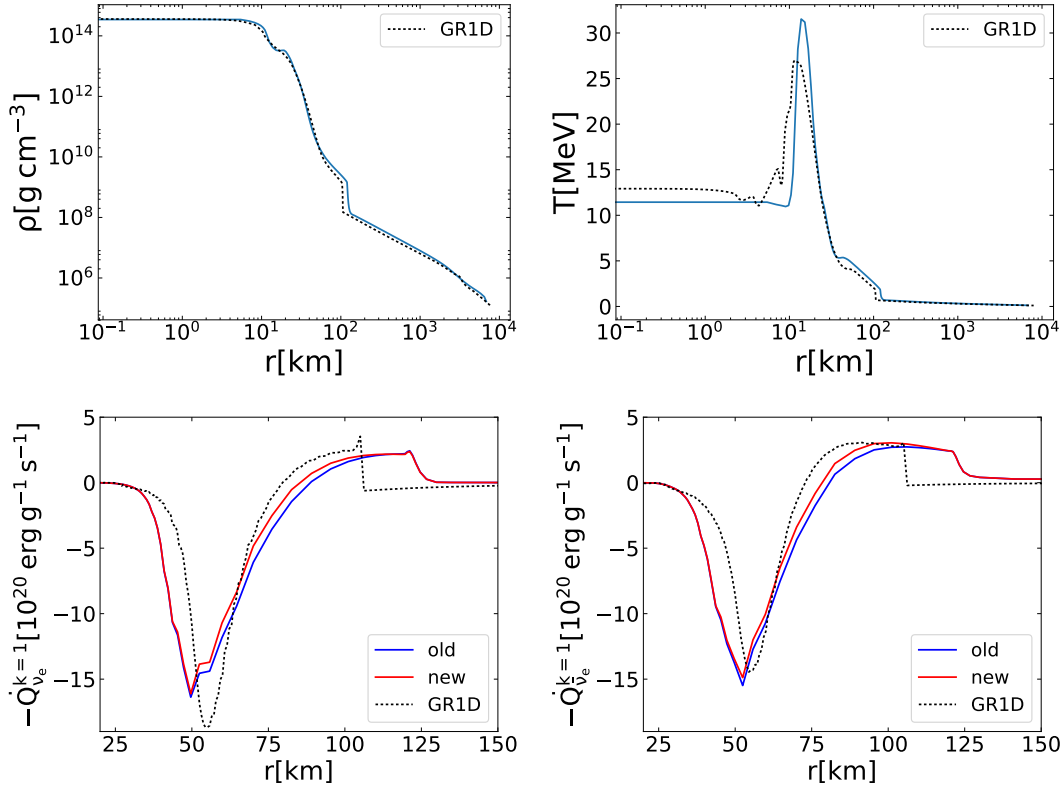


Figure 6. **Top row:** density (left panel) and temperature (right panel) profiles as in Figure 1 but with the addition of the data from the GR1D run. **Bottom row:** Measure of the heating rate in units of $10^{20} \text{ erg g}^{-1} \text{ s}^{-1}$ along the radial profile for electron neutrinos (left panel) and anti-neutrinos (right panel) with the old (blue) and new (red) prescription for the flux factor. An overall good agreement between the two choices of flux factor is visible, with differences at the level of few percents. Positive values mark the dominance of neutrino absorption over emission which can be seen behind the shock location at ~ 120 km. The dashed line shows the result from a dynamical simulation with GR1D.

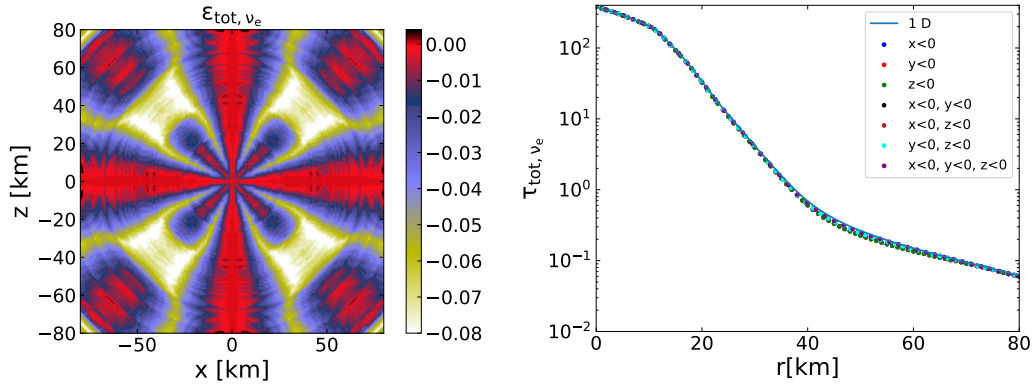


Figure 7. **Left panel:** Relative error $\epsilon_{\nu} = \frac{\tau_{1D} - \tau_{3D}}{\tau_{1D}}$ of the total optical depth for electron neutrinos of energy 10.08 MeV. The 1D values of the optical depth on the plane are obtained by creating a similar 1D profile to the one of Sec. 3.1 but with uniform resolution of 1 km, by integrating over this path, and by mapping the resulting values on the plane itself. For the 3D calculations we use the approach explained in Sec. 2.2. The 3D implementation generally overestimates the optical depths by $\sim 8\%$ at the most. **Right panel:** Total optical depth along the radius from the centre for electron neutrinos of 10.08 MeV. Unlike the 1D profile of uniform resolution adopted in the left panel to obtain the relative error, the blue line corresponds to an integration performed over the 1D profile of variable resolution of Sec. 3.1, while the dots correspond to a selection of radial paths on the 3D grid. ' $x < 0$ ', ' $y < 0$ ' and ' $z < 0$ ' are the paths along the $x < 0, y < 0$ and $z < 0$ axis. ' $x < 0, y < 0$ ' is the diagonal path on the $z = 0$ plane with negative x and y coordinates and $x = y$, ' $x < 0, z < 0$ ' is the diagonal path on the $y = 0$ plane with negative x and z coordinates and $x = z$, ' $y < 0, z < 0$ ' is the diagonal path on the $x = 0$ plane with negative y and z coordinates and $y = z$, ' $x < 0, y < 0, z < 0$ ' is the diagonal path with negative x, y and z coordinates and $x = y, x = z$ and $y = z$. The calculation of the optical depth along the 1D profile of variable resolution leads to a $\lesssim 10\%$ larger optical depth at $\sim 40 - 60$ km from the centre compared to the 3D implementation.

Table 1. Summary of the values of neutrino luminosities and average energies with ASL for both prescriptions of flux factors and for both 1D and 3D implementations. Considering the comparison with the 1D implementation of Sec. 3.1, the 3D implementation provides electron neutrino and anti-neutrino luminosities larger by $\sim 7-8\%$ with the new choice of flux factor. Heavy lepton neutrinos are less affected with a discrepancy of $\sim 1\%$ instead. Similar trend is observed with the old flux factor prescription, with deviations reaching $\sim 10\%$ for electron neutrinos and anti-neutrinos. Such discrepancies reduce to $\sim 3-4\%$ and to $\sim 1-2\%$ with old and new prescription respectively when comparing with the same 1D radial profile but with uniform resolution of 1 km. Comparing the two flux factor prescriptions in 3D, the new one provides electron neutrino and anti-neutrino luminosities $\sim 6-7\%$ smaller than the old one. The 1D comparison between the two flux factor choices provides a slightly lower percentage of $\sim 4-5\%$ instead. Overall, discrepancies in the average energies are of the order of $\lesssim 1-2\%$. We additionally show the values obtained by performing the same calculations with the M1 scheme of GR1D.

Implementation	flux factor, old choice	flux factor, new choice
1D, variable resolution, ASL	$L_{\nu_e}^1 = 4.70 \cdot 10^{52} \text{ erg s}^{-1}$	$L_{\nu_e}^1 = 4.50 \cdot 10^{52} \text{ erg s}^{-1}$
	$L_{\bar{\nu}_e}^1 = 4.61 \cdot 10^{52} \text{ erg s}^{-1}$	$L_{\bar{\nu}_e}^1 = 4.43 \cdot 10^{52} \text{ erg s}^{-1}$
	$L_{\nu_x}^1 = 2.04 \cdot 10^{52} \text{ erg s}^{-1}$	$L_{\nu_x}^1 = 2.04 \cdot 10^{52} \text{ erg s}^{-1}$
	$\langle E_{\nu_e} \rangle = 12.86 \text{ MeV}$	$\langle E_{\nu_e} \rangle = 12.77 \text{ MeV}$
	$\langle E_{\bar{\nu}_e} \rangle = 15.69 \text{ MeV}$	$\langle E_{\bar{\nu}_e} \rangle = 15.52 \text{ MeV}$
	$\langle E_{\nu_x} \rangle = 20.35 \text{ MeV}$	$\langle E_{\nu_x} \rangle = 20.35 \text{ MeV}$
1D, uniform resolution of 1 km, ASL	$L_{\nu_e}^1 = 5.00 \cdot 10^{52} \text{ erg s}^{-1}$	$L_{\nu_e}^1 = 4.76 \cdot 10^{52} \text{ erg s}^{-1}$
	$L_{\bar{\nu}_e}^1 = 4.88 \cdot 10^{52} \text{ erg s}^{-1}$	$L_{\bar{\nu}_e}^1 = 4.67 \cdot 10^{52} \text{ erg s}^{-1}$
	$L_{\nu_x}^1 = 2.01 \cdot 10^{52} \text{ erg s}^{-1}$	$L_{\nu_x}^1 = 2.01 \cdot 10^{52} \text{ erg s}^{-1}$
	$\langle E_{\nu_e} \rangle = 12.98 \text{ MeV}$	$\langle E_{\nu_e} \rangle = 12.82 \text{ MeV}$
	$\langle E_{\bar{\nu}_e} \rangle = 15.72 \text{ MeV}$	$\langle E_{\bar{\nu}_e} \rangle = 15.56 \text{ MeV}$
	$\langle E_{\nu_x} \rangle = 20.33 \text{ MeV}$	$\langle E_{\nu_x} \rangle = 20.33 \text{ MeV}$
3D, uniform resolution of 1 km, ASL	$L_{\nu_e}^1 = 5.17 \cdot 10^{52} \text{ erg s}^{-1}$	$L_{\nu_e}^1 = 4.82 \cdot 10^{52} \text{ erg s}^{-1}$
	$L_{\bar{\nu}_e}^1 = 5.11 \cdot 10^{52} \text{ erg s}^{-1}$	$L_{\bar{\nu}_e}^1 = 4.79 \cdot 10^{52} \text{ erg s}^{-1}$
	$L_{\nu_x}^1 = 2.01 \cdot 10^{52} \text{ erg s}^{-1}$	$L_{\nu_x}^1 = 2.01 \cdot 10^{52} \text{ erg s}^{-1}$
	$\langle E_{\nu_e} \rangle = 12.89 \text{ MeV}$	$\langle E_{\nu_e} \rangle = 12.63 \text{ MeV}$
	$\langle E_{\bar{\nu}_e} \rangle = 15.77 \text{ MeV}$	$\langle E_{\bar{\nu}_e} \rangle = 15.50 \text{ MeV}$
	$\langle E_{\nu_x} \rangle = 20.17 \text{ MeV}$	$\langle E_{\nu_x} \rangle = 20.17 \text{ MeV}$
GR1D, M1	$L_{\nu_e}^1 = 4.20 \cdot 10^{52} \text{ erg s}^{-1}$	
	$L_{\bar{\nu}_e}^1 = 4.10 \cdot 10^{52} \text{ erg s}^{-1}$	
	$L_{\nu_x}^1 = 1.90 \cdot 10^{52} \text{ erg s}^{-1}$	
	$\langle E_{\nu_e} \rangle = 13.30 \text{ MeV}$	
	$\langle E_{\bar{\nu}_e} \rangle = 16.40 \text{ MeV}$	
		$\langle E_{\nu_x} \rangle = 18.90 \text{ MeV}$

Table 2. Variation of the neutrino luminosities and average energies by changing the number of energy bins in the interval $[3, 300] \text{ MeV}$. Choosing a number of energy bins larger than ~ 10 leads to stable values, whereas fewer bins cause notable deviations.

Energy bins	$L_{\nu_e}^1 (\text{erg s}^{-1})$	$L_{\bar{\nu}_e}^1 (\text{erg s}^{-1})$	$L_{\nu_x}^1 (\text{erg s}^{-1})$	$\langle E_{\nu_e} \rangle (\text{MeV})$	$\langle E_{\bar{\nu}_e} \rangle (\text{MeV})$	$\langle E_{\nu_x} \rangle (\text{MeV})$
5	$3.43 \cdot 10^{52}$	$3.36 \cdot 10^{52}$	$1.67 \cdot 10^{52}$	11.66	15.45	18.88
10	$4.45 \cdot 10^{52}$	$4.43 \cdot 10^{52}$	$2.00 \cdot 10^{52}$	12.71	15.59	20.13
15	$4.59 \cdot 10^{52}$	$4.48 \cdot 10^{52}$	$2.02 \cdot 10^{52}$	12.78	15.57	20.25
20	$4.54 \cdot 10^{52}$	$4.48 \cdot 10^{52}$	$2.04 \cdot 10^{52}$	12.77	15.52	20.35
25	$4.65 \cdot 10^{52}$	$4.51 \cdot 10^{52}$	$2.01 \cdot 10^{52}$	12.88	15.57	20.22
30	$4.66 \cdot 10^{52}$	$4.55 \cdot 10^{52}$	$2.05 \cdot 10^{52}$	12.88	15.62	20.41
35	$4.57 \cdot 10^{52}$	$4.53 \cdot 10^{52}$	$2.03 \cdot 10^{52}$	12.77	15.59	20.34
40	$4.66 \cdot 10^{52}$	$4.56 \cdot 10^{52}$	$2.03 \cdot 10^{52}$	12.89	15.64	20.34
45	$4.62 \cdot 10^{52}$	$4.55 \cdot 10^{52}$	$2.04 \cdot 10^{52}$	12.82	15.61	20.38
50	$4.62 \cdot 10^{52}$	$4.55 \cdot 10^{52}$	$2.03 \cdot 10^{52}$	12.83	15.61	20.37
55	$4.58 \cdot 10^{52}$	$4.57 \cdot 10^{52}$	$2.04 \cdot 10^{52}$	12.82	15.63	20.40
60	$4.66 \cdot 10^{52}$	$4.53 \cdot 10^{52}$	$2.04 \cdot 10^{52}$	12.86	15.58	20.41

Table 3. Variation of the luminosities and average energies for all neutrino species considered, with 20 energy bins in total but varying the energy interval. A stability is seen as long as the energy interval is between few MeV to few hundreds MeV. Either a restriction of the interval to energies below ~ 75 MeV or above ~ 10 MeV causes sensitive variations in either the luminosities or the average energies, or both. Note that although a convergence in the luminosities is already seen for energies above ~ 75 MeV, dynamical simulations would also require neutrino energies above ~ 100 MeV to properly model the neutrino trapped components.

Energy range (MeV)	$L_{\nu_e}^1$ (erg s $^{-1}$)	$L_{\bar{\nu}_e}^1$ (erg s $^{-1}$)	$L_{\nu_x}^1$ (erg s $^{-1}$)	$\langle E_{\nu_e} \rangle$ (MeV)	$\langle E_{\bar{\nu}_e} \rangle$ (MeV)	$\langle E_{\nu_x} \rangle$ (MeV)
[3, 30]	$4.35 \cdot 10^{52}$	$4.13 \cdot 10^{52}$	$1.08 \cdot 10^{52}$	12.58	15.07	14.37
[3, 50]	$4.53 \cdot 10^{52}$	$4.44 \cdot 10^{52}$	$1.78 \cdot 10^{52}$	12.78	15.54	18.86
[3, 75]	$4.54 \cdot 10^{52}$	$4.48 \cdot 10^{52}$	$2.01 \cdot 10^{52}$	12.81	15.58	20.22
[3, 100]	$4.59 \cdot 10^{52}$	$4.48 \cdot 10^{52}$	$2.03 \cdot 10^{52}$	12.83	15.55	20.35
[3, 150]	$4.56 \cdot 10^{52}$	$4.44 \cdot 10^{52}$	$2.02 \cdot 10^{52}$	12.77	15.53	20.27
[3, 200]	$4.60 \cdot 10^{52}$	$4.44 \cdot 10^{52}$	$2.04 \cdot 10^{52}$	12.81	15.51	20.35
[3, 250]	$4.64 \cdot 10^{52}$	$4.43 \cdot 10^{52}$	$2.01 \cdot 10^{52}$	12.85	15.49	20.24
[3, 300]	$4.50 \cdot 10^{52}$	$4.43 \cdot 10^{52}$	$2.04 \cdot 10^{52}$	12.71	15.54	20.35
[3, 350]	$4.53 \cdot 10^{52}$	$4.44 \cdot 10^{52}$	$2.05 \cdot 10^{52}$	12.76	15.50	20.38
[3, 400]	$4.59 \cdot 10^{52}$	$4.42 \cdot 10^{52}$	$2.01 \cdot 10^{52}$	12.84	15.50	20.18
[3, 450]	$4.56 \cdot 10^{52}$	$4.45 \cdot 10^{52}$	$2.05 \cdot 10^{52}$	12.76	15.54	20.38
[3, 500]	$4.44 \cdot 10^{52}$	$4.40 \cdot 10^{52}$	$2.02 \cdot 10^{52}$	12.66	15.46	20.26
[3, 550]	$4.55 \cdot 10^{52}$	$4.43 \cdot 10^{52}$	$2.04 \cdot 10^{52}$	12.77	15.52	20.04
[3, 600]	$4.54 \cdot 10^{52}$	$4.39 \cdot 10^{52}$	$2.05 \cdot 10^{52}$	12.74	15.45	20.36
[10, 300]	$4.03 \cdot 10^{52}$	$4.22 \cdot 10^{52}$	$1.96 \cdot 10^{52}$	15.62	17.33	25.39
[15, 300]	$2.84 \cdot 10^{52}$	$3.31 \cdot 10^{52}$	$1.84 \cdot 10^{52}$	19.54	20.30	29.65
[25, 300]	$9.38 \cdot 10^{51}$	$1.23 \cdot 10^{52}$	$1.52 \cdot 10^{52}$	29.38	28.65	37.78

our optical depth algorithm overall captures the actual path that minimises the optical depth and that neutrinos preferentially cross, i.e. the radial path. Obviously the larger the energy the larger the radius of the neutrinosphere, since $\tau_\nu \sim E_\nu^2$. Comparing between species, heavy-lepton neutrinos have smaller energy neutrinospheres because the only interactions where they exchange energy with the fluid are pair processes and bremsstrahlung. On the contrary, elastic scattering on nucleons and nuclei makes the total neutrino surfaces comparable with the other species. Electron neutrinos and anti-neutrinos show similar energy and total neutrinospheres as a result of the comparable amount of emission and absorption interactions involving both species at this time of the post-bounce phase. Moreover, for each of these neutrino species we notice comparable radii of total and energy neutrino surface at each energy, indicating that neutrino emission and absorption reactions, efficient in thermalizing neutrinos, provide also an important opacity contribution to the total optical depth. Overall, the total neutrino surfaces extend from ~ 27 km to ~ 121 km for electron neutrinos, from ~ 25 km to ~ 121 km for electron anti-neutrinos, and from ~ 25 km to ~ 118 km for heavy-lepton neutrinos. Accordingly, the energy surfaces extend from ~ 26 km to ~ 121 km for electron neutrinos, from ~ 24 km to ~ 121 km for electron anti-neutrinos, and from ~ 23 km to ~ 69 km for heavy-lepton neutrinos.

Heating

Calculation of the absorption rates on the grid is done by applying Eq. (6). Computation of the neutrino density is performed by means of Eq. (34) with $\beta_\nu = 0$ (i.e. Eq. (8)) and of Eq. (9). Given the spherical symmetry (see Figure 8) the value of $l_\nu(E, R)$ over the grid is approximately recovered by integrating Eq. (9) over a reference radial path from the origin, and by mapping the obtained values on the path over the rest of the grid. Figure 9 shows the heating rate for electron neutrinos and anti-neutrinos on the plane $y=0$ with the new flux factor prescription in units

of $10^{20} \text{ erg g}^{-1} \text{ s}^{-1}$, resembling the values from Figure 6. Moving outward from the centre, the net rate decreases and reaches its minimum at $\sim 50 - 60$ km from the centre, then increasing and getting to positive values where neutrino heating dominates between 80 km and 120 km. Unlike Figure 6 we notice a slightly lower minimum that goes below $-17.5 \cdot 10^{20} \text{ erg g}^{-1} \text{ s}^{-1}$ and $-15 \cdot 10^{20} \text{ erg g}^{-1} \text{ s}^{-1}$ for electron neutrinos and anti-neutrinos respectively, and a larger maximum above $\sim 2.5 \cdot 10^{20} \text{ erg g}^{-1} \text{ s}^{-1}$ for the heating. This is expected because the original profile of Sec. 3.1 has decreasing resolution with increasing distance from the centre, leading to larger optical depths in the transition between the optically thick and the optically thin regime. This is clearly visible in the right panel of Figure 7, where we plot the total optical depth for electron neutrinos of energy 10.08 MeV (taken as reference) calculated by integrating along the profile of Sec. 3.1 (blue line), together with values of the optical depth calculated along several paths of the 3D grid. In the range $\sim 40 - 60$ km the 1D optical depth is $\lesssim 10\%$ larger than the 3D ones. The lower values from the 3D calculations lead to lower diffusion timescales and therefore to stronger emission and absorption rates.

Neutrino luminosities and average-rms energies

Given the heating rate, we calculate the total neutrino luminosities and average energies. The results are shown in the third row of Table 1. Differences with respect to the 1D case (Sec. 3.1) are of the order of $\sim 7 - 8\%$ for the electron neutrino and anti-neutrino luminosities, and of $\sim 1\%$ for the heavy-lepton neutrinos. Average energies all differ by $\lesssim 1\%$. Considering the results with the old flux factor prescription, differences in the luminosities compared to the 1D case are of the order of $\sim 10\%$ for electron neutrinos and anti-neutrinos and $\sim 1\%$ for heavy lepton neutrinos. In addition, we repeat the calculation for the case of a 1D radial profile with uniform resolution of 1 km. Results are shown in the second row of Table 1. Errors in the luminosities between the 3D and the 1D implementation reduce to $\sim 3 - 4\%$

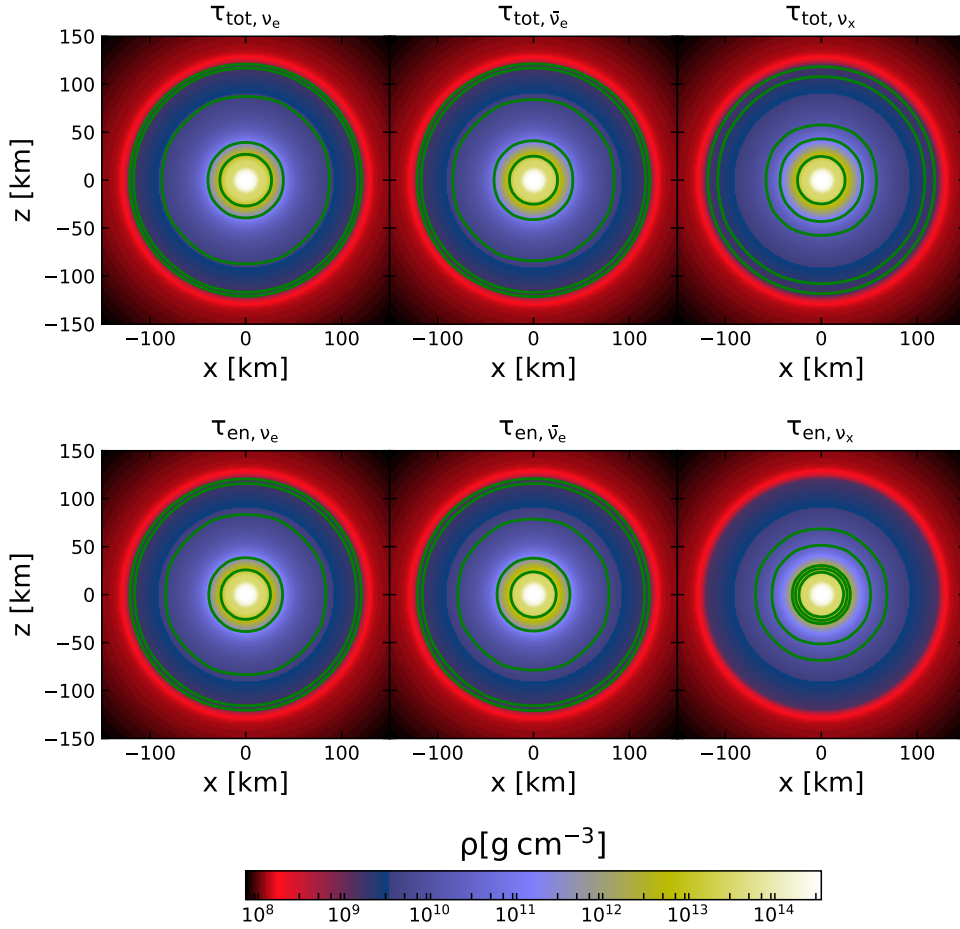


Figure 8. Location of the neutrino surfaces on the density map at $y=0$ for the same sets of neutrino energies used in Figures 3 and 4. **Top row:** total optical depth and **Bottom row:** energy optical depth. For each row, we show electron neutrino (left panel), electron anti-neutrino (middle panel) and heavy-lepton neutrino (right panel). The location of the neutrinosphere is shown in green circles, starting from the inner one at $E=3$ MeV to the outer one at $E=300$ MeV, i.e. neutrino surface radii increase with neutrino energy. While electron neutrinos and anti-neutrinos have similar neutrinosphere radii at all energies both in the total and in the energy optical depths, heavy-lepton neutrinos show smaller energy neutrinospheres than the other species because the only inelastic contribution comes from pair processes and bremsstrahlung. On the other hand, elastic scattering on nuclei and nucleons extends the heavy lepton total surfaces to radii comparable with the other species. Comparable radii of total and energy neutrino surfaces for electron neutrinos and anti-neutrinos indicate that neutrino emission and absorption reactions, efficient in thermalizing neutrinos, provide also an important opacity contribution to the total optical depth.

and to $\sim 1 - 2\%$ with the old and new flux factor prescription respectively, confirming that the resolution contributes as source of variability to the outcome of the simulations. As we have similarly seen already in Sec. 3.1, the choice of the new flux factor in our 3D simulations provides luminosities $\lesssim 6-7\%$ lower respect to the old prescription, while average energies are less affected with discrepancies of $\lesssim 2\%$. Overall, we state that the modification adopted to the standard ASL of Perego et al. (2016) perform well in the context of core-collapse supernova, although more precise assessments require full dynamical evolutions.

3.2.2 Neutron star merger remnants in 3D

As a final 3D test we apply our new scheme to the remnant of a neutron star merger. We start from a snapshot of a merger remnant ($t=38$ ms after merger; Rosswog et al.

(2017)) that has been obtained using the SPH method with the grey leakage scheme of Rosswog & Liebendörfer (2003). For general reviews of the SPH method we refer to recent reviews (Monaghan 2005; Rosswog 2009, 2015). We use the snapshot as a background on which to evolve the neutrino properties until a steady state is reached. Unlike the core-collapse supernovae case, we do not have any information on the neutrino trapped components at this time and therefore we perform our tests by assuming $Y_\nu = Z_\nu = 0$ as initial condition for neutrinos. Although strictly speaking inconsistent as in the configuration trapped neutrinos should already be present, our choice of such initial condition is justified by several arguments. First, the role of the neutrino trapped components is mainly important when doing full dynamical evolutions and in particular it has been shown recently (Perego et al. 2019) that they only marginally affect the thermodynamical

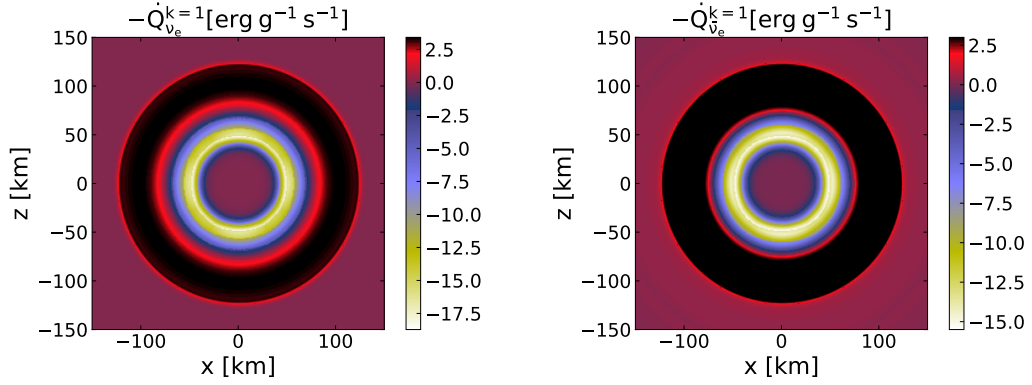


Figure 9. Estimate of the heating rate on the $y=0$ in units of $10^{20} \text{ erg g}^{-1} \text{ s}^{-1}$ with the new flux factor prescription used for the modelling of the heating, for electron neutrinos (left) and anti-neutrinos (right). The values are in agreement with Figure 6, with a positive rate between ~ 80 and ~ 120 km from the origin. However, a stronger neutrino emission and absorption are observed with respect to the 1D implementation as a result of lower optical depths leading to stronger diffusion rates in the transition from diffusion to free streaming.

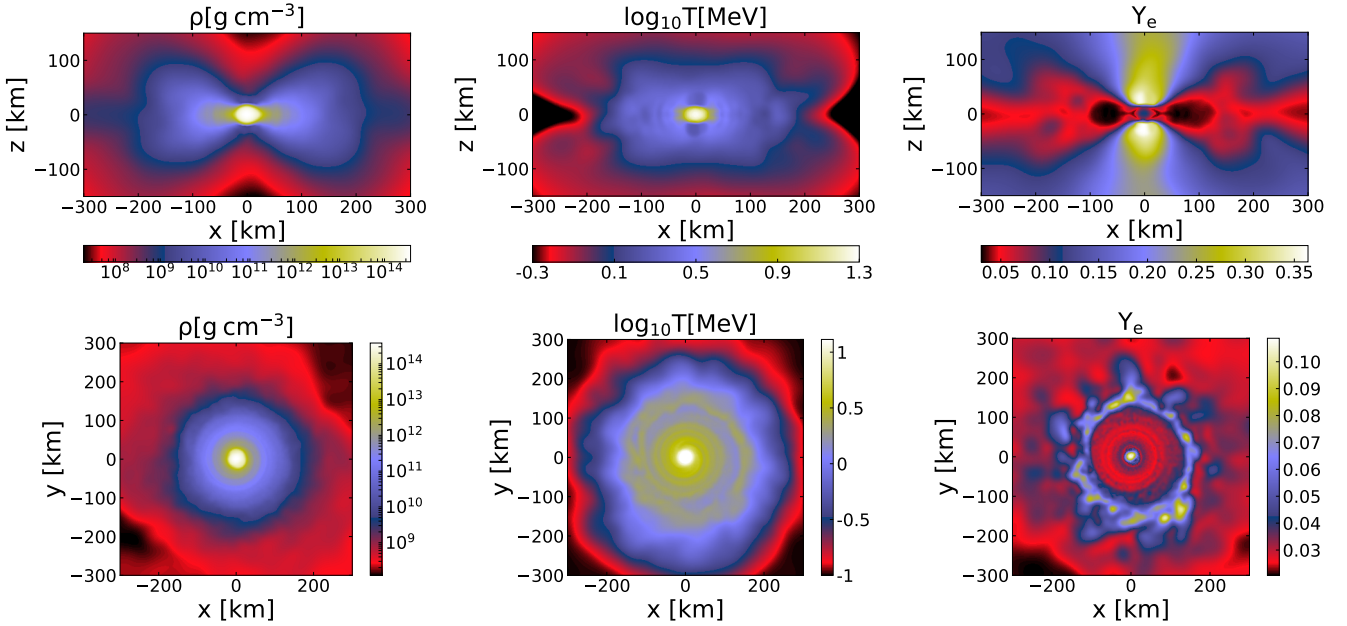


Figure 10. Density (left panels), temperature (middle panels) and electron fraction (right panels) distribution of a $1.4\text{-}1.4 M_{\odot}$ binary neutron star merger configuration at 38 ms after merger. **Top row:** plane $y=0$, **Bottom row:** plane $z=0$. The hot central object is confined within a region of ~ 20 km from the centre and has a mass $\approx 2.3 M_{\odot}$, densities $\rho \sim 3 \cdot 10^{14} \text{ g cm}^{-3}$, temperatures $T \sim 20$ MeV and electron fractions $Y_e \sim 0.1$. The surrounding torus has electron fractions $Y_e < 0.1$ and can be divided in an inner region with densities $\rho \sim 10^{12} - 10^{13} \text{ g cm}^{-3}$ and temperatures $T \sim 3 - 5$ MeV confined within ~ 100 km from the centre, and an outer region up to ~ 200 km with densities $\rho \sim 10^{10} - 10^{11} \text{ g cm}^{-3}$ and temperatures $T \sim 1$ MeV. Larger electron fractions $Y_e \sim 0.2 - 0.3$ are located along the z -axis with a maximum of $Y_e \sim 0.35$ right above the central object, densities $\rho \sim 10^8 \text{ g cm}^{-3}$ and temperatures $T \lesssim 1$ MeV.

properties of the remnant, and only close to the merger time where neutrinos are produced in the first place. Second, setting $Y_{\nu} = Z_{\nu} = 0$ implies a remnant configuration out of equilibrium, and given the large temperature dependence of the neutrino-matter cross sections (Bruenn 1985; Burrows & Thompson 2004) the system rapidly reaches a new state by refilling the neutrino fractions over a timescale $Y_{\nu}/\dot{Y}_{\nu} \lesssim 10^{-6}$ s, which is much less than the typical dynamical timescale of the remnant $\sim (\bar{G}\rho)^{-1/2} \approx 2 \cdot 10^{-4}$ s. Third, absorption under optically thin conditions (that we are modeling here) is led by non-trapped neutrinos. For all the above reasons,

we do not expect the modeling of the trapped neutrinos to have a significant impact on our calculations. The neutron stars have been discretized with $N \sim 1$ million particles and the initial conditions are mapped on a 3D grid whose borders are defined when densities go below $\sim 10^8 \text{ g cm}^{-3}$. Figure 10 shows the density, temperature and electron fraction on the planes $y=0$ and $z=0$. The central object has a mass $\approx 2.3 M_{\odot}$, densities $\rho \sim 3 \cdot 10^{14} \text{ g cm}^{-3}$, temperatures $T \sim 20$ MeV and electron fractions $Y_e \sim 0.1$. Around it is a torus with $Y_e < 0.1$, an inner region with densities $\rho \sim 10^{12} - 10^{13} \text{ g cm}^{-3}$ and temperatures $T \sim 3 - 5$ MeV, and

Table 4. Summary of the neutrino luminosities and average energies for electron neutrinos, electron anti-neutrinos and heavy-lepton neutrinos, calculated with ASL (second column) and M1 (third column), for the binary merger snapshot at ~ 38 ms after merger.

Quantity	ASL	M1
$L_{\nu_e}(\text{erg s}^{-1})$	$1.64 \cdot 10^{52}$	$2.56 \cdot 10^{52}$
$L_{\bar{\nu}_e}(\text{erg s}^{-1})$	$1.69 \cdot 10^{52}$	$2.28 \cdot 10^{52}$
$L_{\nu_x}(\text{erg s}^{-1})$	$7.64 \cdot 10^{51}$	$7.50 \cdot 10^{51}$
$\langle E_{\nu_e} \rangle (\text{MeV})$	13.10	15.46
$\langle E_{\bar{\nu}_e} \rangle (\text{MeV})$	13.59	12.86
$\langle E_{\nu_x} \rangle (\text{MeV})$	14.09	15.50

an outer region with densities $\rho \sim 10^{10} - 10^{11} \text{ g cm}^{-3}$ and temperatures $T \sim 1$ MeV. Electron fractions $Y_e \sim 0.2 - 0.3$ are located along the low-density polar region.

3D optical depth

Computation of the neutrino properties requires the calculation of the optical depth on the grid as explained in Sec. 2.2. Figure 11 shows the location of the total and energy neutrino surfaces for the same sets of energies used for the core-collapse supernovae tests (see Figures 3 and 4). Overall, we see an agreement with the distribution of the surfaces described in Perego et al. (2014).

As already noticed for the core-collapse supernovae case, the higher the energy of neutrinos the more extended the neutrino surface. Accordingly, the heavy-lepton neutrinos have less extended energy than total neutrino surfaces because they can only exchange energy by pair processes and bremsstrahlung. Elastic scattering on nuclei and nucleons make the heavy lepton total neutrino surfaces comparable with the ones of the other species. Electron neutrinos again show comparable energy and total neutrino surfaces due to the neutron rich environment that favours energy exchange in processes like neutrino absorption on neutrons. However, we notice that compared to the core-collapse supernova case electron anti-neutrinos show less extended total and energy neutrino surfaces compared to the corresponding electron neutrino ones as a consequence of the low abundance of free protons.

Heating

The heating is modelled by Eqs. (6) and (34) and by estimating β_ν as described in Sec. 2.2. To save computational time, we limit our transport calculation to those regions where density is above 10^9 g cm^{-3} . Indeed, we find that the contribution at lower densities affect the transport quantities by less than 1%. For the computation of $l_\nu(E, \mathbf{x})$ we create a 1D profile of 1 km of resolution where to each bin of radius R_{bin} we assign a neutrino emission by summing up the contribution of all grid points with radial distance from the centre within that bin. We then solve Eq. (9) and assign the same $l_\nu(E, R_{\text{bin}})$ to all grid points inside that bin. In this way we create a spherically symmetric neutrino emission by coupling fluid points from the torus with fluid points along the poles, and we then leave to β_ν the task of approximately recovering the degree of anisotropy of the system and consequently the degree of decoupling between points at same distance from the centre but at different polar angles. The determination of the exponent b in

Eq. (34) is performed by comparing with an M1 calculation of the heating from FLASH. In particular, we find $b = 8$ to overall best recover the electron neutrino contribution to the heating (which constitutes more than 50% of the total) and we therefore assume the same value for the corresponding anti-neutrinos as well.

In Figure 12 we show the angular dependence of the neutrino flux, i.e. $\Lambda_\nu(\theta)$ vs θ , calculated from Eq. (2.2.3) with $\Delta\theta = 10^\circ$ ⁵. We notice that the modulation of the flux with the polar angle is more pronounced for electron neutrinos than for electron anti-neutrinos. This is due to the fact that the neutron rich torus is more opaque to electron neutrinos than to electron anti-neutrinos. Therefore, the electron neutrino flux points mostly along the z-direction. In terms of neutrino emission, the largest contribution to the cooling for the electron neutrinos ($\sim 10^{21} \text{ erg g}^{-1} \text{ s}^{-1}$) is confined within radii $\lesssim 20$ km from the centre, and the remaining subdominant part ($\sim 10^{19} - 10^{20} \text{ erg g}^{-1} \text{ s}^{-1}$) occurs inside the torus. We find that electron anti-neutrinos in contrast are mostly emitted in the torus (cooling $\sim 10^{20} \text{ erg g}^{-1} \text{ s}^{-1}$) and no relevant emission is found at radii $\lesssim 20$ km from the centre. We obtain $\beta_{\nu_e} \approx 16$ and $\beta_{\bar{\nu}_e} \approx 2$. In the first row of Figure 13 we show 2D maps of the resulting heating rate on the plane $y = 0$. In the second row we show the same maps for calculations performed with the M1 scheme implemented in FLASH. The major contribution to the heating is located within $\sim 45^\circ$ from the pole for both species. The largest differences of the ASL compared to M1 are in the region with $\theta \lesssim 45^\circ$, and in particular above the central object at $\theta \lesssim 15^\circ$, where the electron neutrino and anti-neutrino heating are respectively lower by a factor of ~ 1.5 and larger by a factor of ~ 2 . Moreover, unlike the M1 implementation our ASL algorithm provides a residual electron neutrino heating ($\sim 10^{19} - 10^{20} \text{ erg g}^{-1} \text{ s}^{-1}$) at $\theta \sim 60^\circ - 90^\circ$ in regions where $\tau_{\text{tot}} \leq 1$. We notice that both ASL and M1 provide an electron neutrino heating larger by one order of magnitude compared to electron anti-neutrinos. This is due to two effects: first, our snapshot calculations show an electron anti-neutrino cooling which is at the most $\sim 10^{20} \text{ erg g}^{-1} \text{ s}^{-1}$, i.e. one order of magnitude lower than the electron neutrino one, which reaches $\sim 10^{21} \text{ erg g}^{-1} \text{ s}^{-1}$ close to the central remnant where the anti-neutrino emission is negligible in comparison. Second, the neutron rich environment favours the electron neutrino absorption over the corresponding anti-neutrinos.

Neutrino luminosities and average-rms energies

The overall low anti-neutrino cooling leads to almost equal electron neutrino and anti-neutrino total luminosities and average energies, contrarily to what is typically expected from merger simulations (Rosswog & Liebendörfer 2003; Perego et al. 2014; Dessart et al. 2009; Foucart et al. 2016). In particular, a summary of these values is reported in Table 4. The reason for this is most likely due to the application of a different neutrino transport than the one adopted for generating the snapshot. In fact, we further calculate the neutrino cooling with our ASL for a similar snapshot of the merging of two $1.4 M_\odot$ neutron stars

⁵ We have tested different $\Delta\theta$ and no appreciable variations appears in the computation of β_ν , therefore we set $\Delta\theta = 10^\circ$.

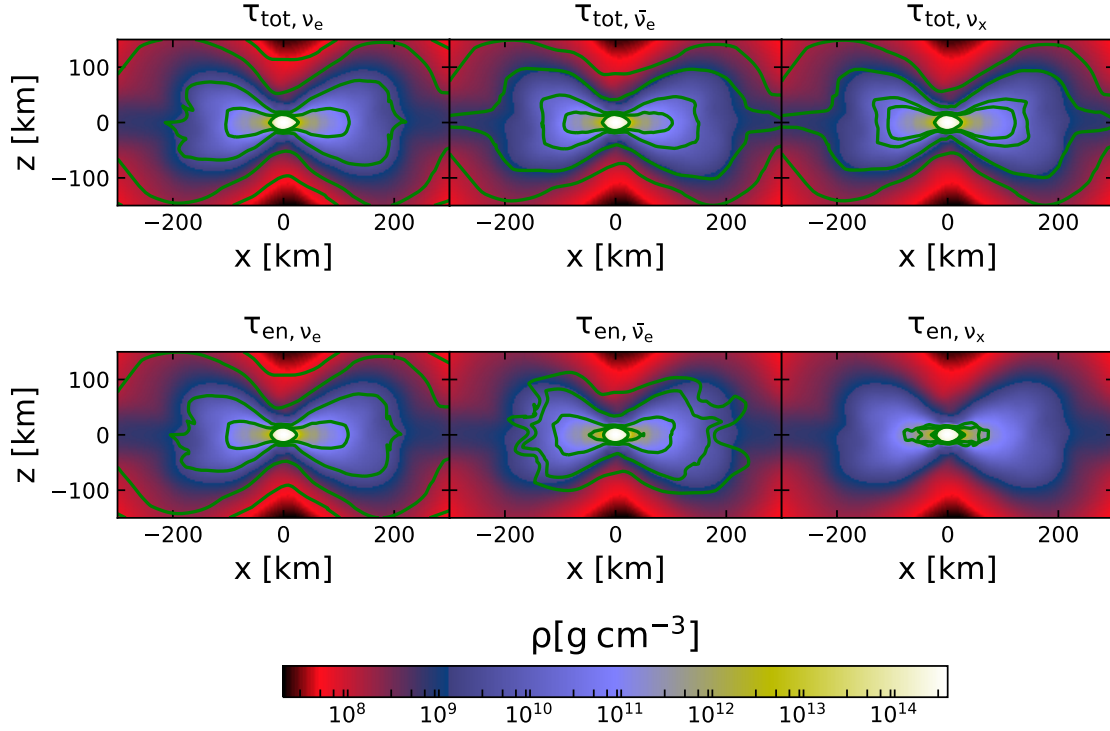


Figure 11. Location of the neutrino surfaces for the same sets of neutrino energies used in Figures 3 and 4. **Top row:** total optical depth and **Bottom row:** energy optical depth. For each row, we show electron neutrino (left panel), electron anti-neutrino (middle panel) and heavy-lepton neutrino (right panel). The location of the neutrino surface is shown in green, starting from the inner one at $E = 3$ MeV to the outer one at $E = 300$ MeV. Note the shape resembling the presence of a torus around the central object and therefore of a non-spherical geometry. Similarities with Figure 8 are visible, both in the distribution of the surfaces with increasing neutrino energy and in the comparison of total and energy optical depths of each species. However, with respect to the core-collapse supernova case, the low abundance of free protons makes the electron anti-neutrino total and energy neutrino surfaces less extended with respect to the electron neutrino ones.

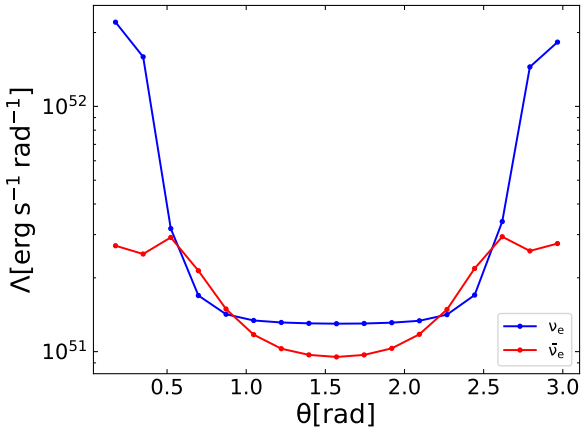


Figure 12. $\Lambda_\nu(\theta)$ as function of θ for electron neutrinos (blue) and anti-neutrinos (red). Electron neutrinos show a more pronounced anisotropy compared to the corresponding anti-neutrinos, with $\beta_{\nu_e} \approx 16$ and $\beta_{\bar{\nu}_e} \approx 2$.

taken from the simulations of Perego et al. (2014) at ~ 66 ms after the first contact of the two stars. The ASL of Perego et al. (2014) is similar to ours, and in particular is spectral. In this case we get $L_{\nu_e}^{\text{cool}} = 1.45 \cdot 10^{52} \text{ erg s}^{-1}$,

$L_{\bar{\nu}_e}^{\text{cool}} = 1.85 \cdot 10^{52} \text{ erg s}^{-1}$, $L_{\nu_x}^{\text{cool}} = 1.34 \cdot 10^{52} \text{ erg s}^{-1}$, $\langle E_{\nu_e} \rangle = 10.81 \text{ MeV}$, $\langle E_{\bar{\nu}_e} \rangle = 14.97 \text{ MeV}$, $\langle E_{\nu_x} \rangle = 16.00 \text{ MeV}$, $E_{\text{rms}, \nu_e} = 12.02 \text{ MeV}$, $E_{\text{rms}, \bar{\nu}_e} = 16.77 \text{ MeV}$, $E_{\text{rms}, \nu_x} = 19.74 \text{ MeV}$, that is, the largest cooling is from the electron anti-neutrinos being the most luminous, and we also clearly recover the expected hierarchies, i.e. $L_{\bar{\nu}_e}^{\text{cool}} > L_{\nu_e}^{\text{cool}} > L_{\nu_x}^{\text{cool}}$, $\langle E_{\nu_x} \rangle > \langle E_{\bar{\nu}_e} \rangle > \langle E_{\nu_e} \rangle$, $E_{\text{rms}, \nu_x} > E_{\text{rms}, \bar{\nu}_e} > E_{\text{rms}, \nu_e}$.⁶ In particular, we observe that the configuration at ~ 66 ms shows larger densities and temperatures at radii $\lesssim 20$ km from the centre compared to the ~ 38 ms one, producing a dominant electron anti-neutrino cooling $\sim 10^{21} \text{ erg g}^{-1} \text{ s}^{-1}$ (see Figure 14 for a comparison done with ASL along $\theta = 0^\circ$) that is instead missing in the configuration at ~ 38 ms. Moreover, the two snapshots have been previously evolved with different neutrino transport schemes: the one at ~ 66 ms with the scheme of Perego et al. (2014) which is similar to our version of the ASL, the ~ 38 ms one with the grey scheme of Rosswog & Liebendörfer (2003). Applying a different neutrino transport than the one used for generating the snapshot introduces inconsistencies that

⁶ Although we recover the expected hierarchies, we do not find the same values of Perego et al. (2014) as they perform a dynamical simulation assuming neither blocking nor thermalization corrections in Eq. (5).

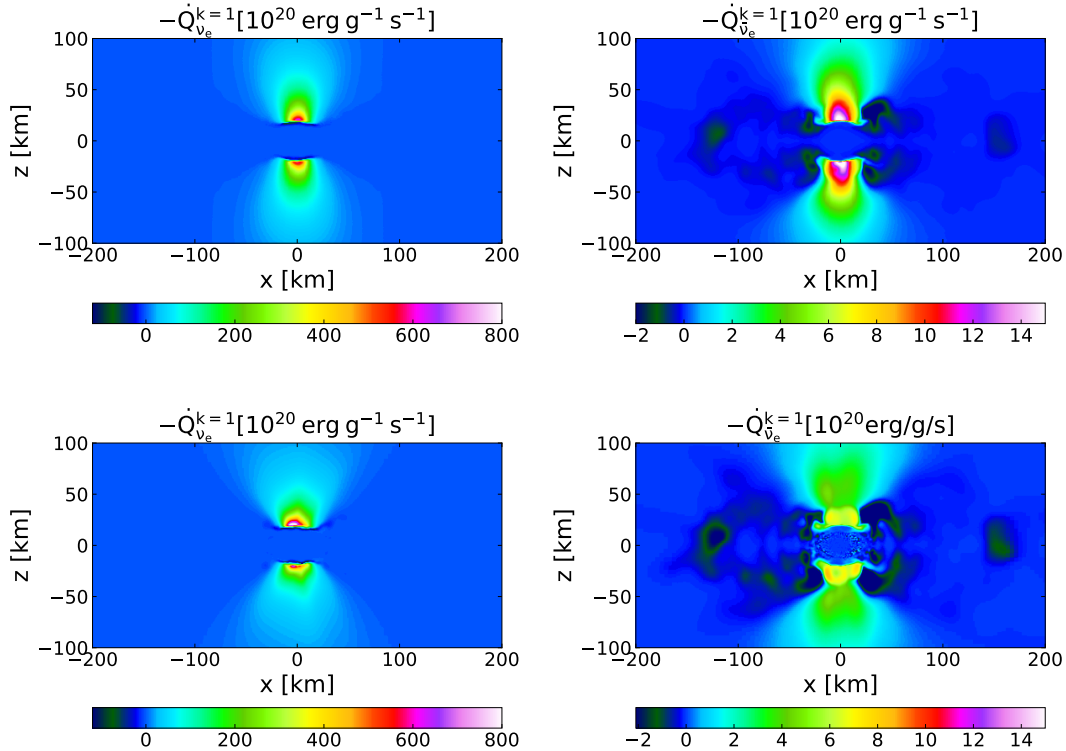


Figure 13. Top row: ASL and Bottom row: M1 heating rate maps on the plane $y=0$ in units of $10^{20} \text{ erg g}^{-1} \text{ s}^{-1}$ for electron neutrinos (right panels) and electron anti-neutrinos (left panels). In both ASL and M1 the electron neutrino cooling occurs mainly close to the central object at distances $\lesssim 20 \text{ km}$ from the centre, while for the electron anti-neutrinos it is mostly located in the torus, where isolated spots of neutrino emission are visible. For both species, the main contribution to the heating is located into a funnel $\sim 45^\circ$ from the pole. Moreover, the electron neutrino heating is generally up to one order of magnitude larger than the electron anti-neutrino one. Compared to M1, the ASL provides an electron neutrino heating rate above the central object at $\theta \lesssim 15^\circ$ lower by a factor ~ 1.5 and a residual contribution at $\theta \sim 60^\circ - 90^\circ$ of about $10^{19} - 10^{20} \text{ erg g}^{-1} \text{ s}^{-1}$ (not appreciable in the Figure), as result of the criterion $\tau_{\text{tot}} \leq 1$, that whenever satisfied triggers neutrino absorption. Furthermore, the electron anti-neutrino heating above the central object at $\theta \lesssim 15^\circ$ is larger by a factor of ~ 2 .

are likely to be the reason for our luminosity values. From Table 4 we notice that the ASL provides electron neutrino and anti-neutrino luminosities lower by $\sim 35\%$ and $\sim 25\%$ respectively in comparison to M1. Average-rms energies agree within $5 - 15\%$. The lower luminosity values from the ASL can be due to several reasons. First, the ASL has excess heating at $\theta \sim 60^\circ - 90^\circ$ for the electron neutrino and at $\theta \sim 15^\circ$ for the electron anti-neutrinos compared to M1. Second, we have kept the values of the ASL parameters entering Eq. (5) to the ones calibrated for core-collapse supernovae simulations. New calibrations are crucial as they might impact the neutrino cooling and consequently the amount of neutrino heating. In particular, the comparison with M1 suggests a lower $\alpha_{\nu, \text{blk}}$. This can be explained in the following way. While in core-collapse supernovae the quasi-spherical symmetry implies that neutrinos move preferentially along the radial direction, in binary mergers neutrinos have more directional freedom in escaping the system and consequently the blocking is expected to be less effective. Third and above all, a more consistent comparison between two neutrino transport approaches would require dynamical evolutions rather than snapshot calculations. Putting together all these uncertainties we find our ASL-M1 luminosity discrepancies, lower than a factor

of 2, a promising initial step toward future developments. We also want to stress that the choice we have made for the flux modulation $\sim \cos^8(\theta)$ is only meant to be a preliminary step toward explorations in full dynamical evolution of binary mergers. Finally, we stress the fact that we have based our heating calculations on the comparison with a moment approach with analytical closure. However, as pointed out by Foucart et al. (2018) the M1 closure can overestimate the neutrino density by up to $\sim 50\%$ along the polar regions, thus limiting the possibility of properly modeling the neutrino driven-winds. Future simulations of binary mergers will definitely need improvements in moment schemes as well for more reliable assessments of the neutrino physics in such systems.

4 SUMMARY

In this paper we have presented an extension of the Advanced Spectral Leakage scheme originally introduced by Perego et al. (2016). Our main goal was to adapt the scheme so that it can be conveniently used for neutron star merger simulations. The main advantage compared to simpler leakage schemes is that the ASL includes neutrino heating pro-

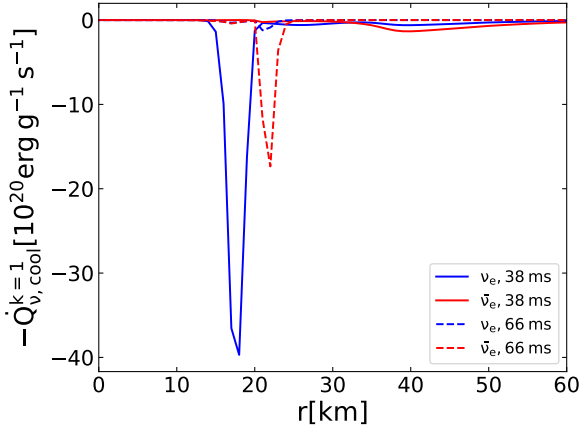


Figure 14. Cooling along the radius at $\theta = 0^\circ$ in units of $10^{20} \text{ erg g}^{-1} \text{ s}^{-1}$ for electron neutrinos (blue) and electron anti-neutrinos (red), for the snapshots at 38 ms and 66 ms, calculated with ASL. While the 38 ms snapshot (solid lines) has negligible anti-neutrino emission in comparison to electron neutrinos, the 66 ms snapshot (dashed lines) shows a dominant anti-neutrino cooling $\sim 10^{21} \text{ erg g}^{-1} \text{ s}^{-1}$ over the electron neutrinos.

cesses and can therefore, with a reasonable computational effort, also model the emergence of neutrino-driven winds in a 3D merger simulation. The main novelty compared to the original approach is the usage of an optical depth-dependent flux factor, and a modification to the equation of the neutrino density in the semi-transparent regime, both designed for the multi-dimensional modeling of compact binary mergers.

We scrutinized the new scheme on the case of a $15 M_\odot$ core-collapse supernova snapshot taken from [Perego et al. \(2016\)](#) at 275 ms after bounce. For this spherically symmetric case we first tested in 1D our new flux factor and found that it agrees well with the original choice ($\lesssim 2\%$ for the average energies and $\lesssim 5\%$ in the neutrino luminosities). As a further 1D test, we have compared the new scheme to the M1 implementation of the GR1D code ([O’Connor & Ott 2010](#); [O’Connor 2015](#)) and here we found agreement, beside differences arising from the usage of different transport schemes. We also mapped the 1D case onto a spherically symmetric, but three-dimensional grid. Here the agreement is slightly worse, but overall still very good: $\lesssim 2\%$ for the average energies and $\lesssim 7\%$ for the neutrino luminosities.

We have finally explored the ASL for an SPH snapshot of a $1.4\text{-}1.4 M_\odot$ binary neutron star merger. As a reference we compared against the results obtained with a M1 scheme that is implemented in FLASH ([Fryxell et al. 2000](#); [O’Connor & Couch 2018](#)). Here, in ASL the anisotropy in the neutrino fluxes is taken into account by an anisotropy parameter β_ν , which is estimated from the ratio between the neutrino fluxes at pole and equator in a similar way as it has been done in [Rosswog & Liebendörfer \(2003\)](#). The neutrino density is modelled $\propto \cos^b(\theta)$, where the value of $b = 8$ is obtained by a comparison of the neutrino heating rate with the M1-FLASH results. Overall, we find good agreement in the neutrino heating distribution between both approaches. The average energies agree within 5-15%. The ASL total luminosities are lower by 25-35% compared to M1. This

discrepancy may suggest that some of the free parameters need to be calibrated more specifically for the case of binary compact mergers. While specific questions may require more sophisticated neutrino transport methods, we are confident that this enhanced ASL scheme delivers reasonably accurate bulk neutrino properties. This will be applied and further tested in future dynamical simulations.

In the tests shown, relativistic effects were neglected. The inclusion of general relativity enhances the gravitational well, leading to more compact and hotter remnants. The energy of the radiation field measured by an observer at a given distance from the emission region is redshifted as neutrinos climb out of the gravitational well. In addition, for relativistic fluid motions the neutrino energy is Doppler shifted depending on the relative velocity between the source and the observer. Simulations of core-collapse supernovae including relativistic effects show an increase in the neutrino luminosities and average energies with respect to the Newtonian case, as well as larger energy-deposition rates by neutrino absorption ([Lentz et al. 2012](#); [Müller et al. 2012](#); [O’Connor & Couch 2018](#)). In the context of compact binary mergers, a larger heating can affect both the amount of neutrino-driven wind ejecta and the reprocessing of the electron fraction in the ejecta. At last, it is worth keeping in mind that most of the neutrino emission in a merger remnant comes from the torus. The orbital velocities of the matter inside of it can be mildly relativistic (e.g. [Foucart et al. \(2015\)](#)). As a consequence, the angular distribution of the neutrino fluxes emitted at the neutrino decoupling surfaces can be sensitively affected by relativistic beaming. In particular, the neutrino emission at the neutrino decoupling surface seen by the observer will be concentrated in a cone directed toward the direction of the fluid motion, rather than being isotropic as seen in the rest frame of the fluid. This can reduce the amount of received flux along the poles with respect to the Newtonian case. The inclusion of all these effects will be the subject of future work.

ACKNOWLEDGEMENTS

This work has been supported by the Swedish Research Council (VR) under grant number 2016- 03657_3, by the Swedish National Space Board under grant number Dnr. 107/16 and by the research environment grant “Gravitational Radiation and Electromagnetic Astrophysical Transients (GREAT)” funded by the Swedish Research council (VR) under Dnr 2016-06012. We would like to thank Sean Couch for major contributions to the development of FLASH. Moreover, we gratefully acknowledge support from COST Action CA16104 “Gravitational waves, black holes and fundamental physics” (GWverse), from COST Action CA16214 “The multi-messenger physics and astrophysics of neutron stars” (PHAROS), and from COST Action MP1304 “Exploring fundamental physics with compact stars (NewCompStar)”.

The simulations were performed on resources provided by the Swedish National Infrastructure for Computing (SNIC) at PDC (Center for High Performance Computing) and NSC (National Supercomputer Centre) and on the resources of the Northern German Supercomputing Alliance (HLRN).

REFERENCES

- Abbott B. P., et al., 2017a, *Physical Review Letters*, **119**, 161101
- Abbott B. P., et al., 2017b, *Nature*, **551**, 85
- Abbott B. P., et al., 2017c, *ApJ*, **848**, L12
- Abbott B. P., et al., 2018, *Physical Review Letters*, **121**, 161101
- Alexander K. D., et al., 2017, *ApJ*, **848**, L21
- Antoniadis J., et al., 2013, *Science*, **340**, 448
- Arcavi I., et al., 2017, *Nature*, **551**, 64
- Ardevol-Pulpillo R., Janka H. T., Just O., Bauswein A., 2019, *MNRAS*, **485**, 4754
- Bruenn S. W., 1985, *ApJS*, **58**, 771
- Bruenn S. W., Buchler J. R., Yueh W. R., 1978, *Ap&SS*, **59**, 261
- Buras R., Janka H.-T., Rampp M., Kifonidis K., 2006, *A&A*, **457**, 281
- Burrows A., Thompson T. A., 2004, in Fryer C. L., ed., *Astrophysics and Space Science Library* Vol. 302, *Astrophysics and Space Science Library*. pp 133–174, doi:10.1007/978-0-306-48599-2.5
- Cabezón R. M., Pan K.-C., Liebendörfer M., Kuroda T., Ebinger K., Heinemann O., Perego A., Thielemann F.-K., 2018, *A&A*, **619**, A118
- Chornock R., et al., 2017, *ApJL*, **848**, L19
- Coughlin M. W., Dietrich T., Margalit B., Metzger B. D., 2018, arXiv e-prints, arXiv:1812.04803,
- Coulter D. A., et al., 2017, *Science*, **358**, 1556
- Cromartie H. T., et al., 2019, arXiv e-prints, arXiv:1904.06759,
- Demorest P. B., Pennucci T., Ransom S. M., Roberts M. S. E., Hessels J. W. T., 2010, *Nature*, **467**, 1081
- Dessart L., Ott C. D., Burrows A., Rosswog S., Livne E., 2009, *ApJ*, **690**, 1681
- Endrizzi A., et al., 2019, arXiv e-prints, arXiv:1908.04952,
- Foucart F., et al., 2015, *Phys. Rev. D*, **91**, 124021
- Foucart F., O'Connor E., Roberts L., Kidder L. E., Pfeiffer H. P., Scheel M. A., 2016, *Phys. Rev. D*, **94**, 123016
- Foucart F., Duez M. D., Kidder L. E., Nguyen R., Pfeiffer H. P., Scheel M. A., 2018, *Phys. Rev. D*, **98**, 063007
- Fryxell B., et al., 2000, *ApJS*, **131**, 273
- Goldstein A., et al., 2017, *ApJ*, **848**, L14
- Haggard D., Nynka M., Ruan J. J., Kalogera V., Cenko S. B., Evans P., Kennea J. A., 2017, *ApJ*, **848**, L25
- Hallinan G., et al., 2017, *Science*, **358**, 1579
- Kasen D., Metzger B., Barnes J., Quataert E., Ramirez-Ruiz E., 2017, *Nature*, **551**, 80
- Kasliwal M. M., Nakar E., Singer L. P., Kaplan D. L., et al. 2017, *Science*, **358**, 1559
- Kasliwal M. M., et al., 2019, *MNRAS*,
- Kilpatrick C. D., et al., 2017, *Science*, **358**, 1583
- Korobkin O., Rosswog S., Arcones A., Winteler C., 2012, *MNRAS*, **426**, 1940
- Lattimer J. M., Douglas Swesty F., 1991, *Nuclear Physics A*, **535**, 331
- Lentz E. J., Mezzacappa A., Messer O. E. B., Liebendörfer M., Hix W. R., Bruenn S. W., 2012, *The Astrophysical Journal*, **747**, 73
- Liebendörfer M., Rosswog S., Thielemann F.-K., 2002, *The Astrophysical Journal Supplement Series*, **141**, 229
- Liebendörfer M., Whitehouse S. C., Fischer T., 2009, *The Astrophysical Journal*, **698**, 1174
- Lindquist R. W., 1966, *Annals of Physics*, **37**, 487
- Margutti R., et al., 2017, *ApJ*, **848**, L20
- Martin D., Perego A., Kastaun W., Arcones A., 2018, *Classical and Quantum Gravity*, **35**, 034001
- Metzger B. D., et al., 2010, *MNRAS*, **406**, 2650
- Mezzacappa A., Messer O. E. B., 1999, *Journal of Computational and Applied Mathematics*, **109**, 281
- Monaghan J. J., 2005, *Reports on Progress in Physics*, **68**, 1703
- Most E. R., Weih L. R., Rezzolla L., Schaffner-Bielich J., 2018, *Physical Review Letters*, **120**, 261103
- Müller B., Janka H.-T., Marek A., 2012, *The Astrophysical Journal*, **756**, 84
- O'Connor E., 2015, *ApJS*, **219**, 24
- O'Connor E. P., Couch S. M., 2018, *The Astrophysical Journal*, **854**, 63
- O'Connor E., Ott C. D., 2010, *Classical and Quantum Gravity*, **27**, 114103
- O'Connor E., Ott C. D., 2013, *ApJ*, **762**, 126
- Pan K.-C., Mattes C., O'Connor E. P., Couch S. M., Perego A., Arcones A., 2018, *Journal of Physics G: Nuclear and Particle Physics*, **46**, 014001
- Perego A., Rosswog S., Cabezón R. M., Korobkin O., Käppeli R., Arcones A., Liebendörfer M., 2014, *MNRAS*, **443**, 3134
- Perego A., Cabezón R. M., Käppeli R., 2016, *ApJS*, **223**, 22
- Perego A., Yasin H., Arcones A., 2017a, *Journal of Physics G Nuclear Physics*, **44**, 084007
- Perego A., Radice D., Bernuzzi S., 2017b, *ApJ*, **850**, L37
- Perego A., Bernuzzi S., Radice D., 2019, arXiv e-prints, arXiv:1903.07898,
- Pian E., et al., 2017, *Nature*, **551**, 67
- Radice D., Perego A., Zappa F., Bernuzzi S., 2018a, *ApJ*, **852**, L29
- Radice D., Perego A., Hotokezaka K., Fromm S. A., Bernuzzi S., Roberts L. F., 2018b, *The Astrophysical Journal*, **869**, 130
- Rosswog S., 2009, *New Astron. Rev.*, **53**, 78
- Rosswog S., 2015, *Living Reviews of Computational Astrophysics* (2015), 1
- Rosswog S., Liebendörfer M., 2003, *MNRAS*, **342**, 673
- Rosswog S., Feindt U., Korobkin O., Wu M.-R., Sollerman J., Goobar A., Martinez-Pinedo G., 2017, *Classical and Quantum Gravity*, **34**, 104001
- Rosswog S., Sollerman J., Feindt U., Goobar A., Korobkin O., Wollaeger R., Fremling C., Kasliwal M. M., 2018, *A&A*, **615**, A132
- Savchenko V., et al., 2017, *ApJ*, **848**, L15
- Schutz B. F., 1986, *Nature*, **323**, 310
- Smartt S. J., et al., 2017, *Nature*, **551**, 75
- Tanvir N. R., et al., 2017, *ApJL*, **848**, L27
- Thorne K. S., 1981, *MNRAS*, **194**, 439
- Troja E., et al., 2017, *Nature*, **551**, 71
- Villar V. A., et al., 2017, *ApJ*, **851**, L21

This paper has been typeset from a \LaTeX file prepared by the author.